CD169(+) macrophages are critical for osteoblast maintenance and promote intramembranous and endochondral ossification during bone repair

Accepted Manuscript

CD169^{+} macrophages are critical for osteoblast maintenance and promote intramembranous and endochondral ossification during bone repair

Lena Batoon, Susan Marie Millard, Martin Eduard Wullschleger, Corina Preda, Andy Chiu-Ku Wu, Simranpreet Kaur, Hsu-Wen Tseng, David Arthur Hume, Jean-Pierre Levesque, Liza Jane Raggatt, Allison Robyn Pettit

PII: S0142-9612(17)30682-8

DOI: 10.1016/j.biomaterials.2017.10.033

Reference: JBMT 18315

To appear in: *Biomaterials*

Received Date: 16 June 2017

Revised Date: 6 September 2017

Accepted Date: 17 October 2017

Please cite this article as: Batoon L, Millard SM, Wullschleger ME, Preda C, Wu AC-K, Kaur S, Tseng H-W, Hume DA, Levesque J-P, Raggatt LJ, Pettit AR, CD169^{+} macrophages are critical for osteoblast maintenance and promote intramembranous and endochondral ossification during bone repair, *Biomaterials* (2017), doi: 10.1016/j.biomaterials.2017.10.033.

CD169^{+} macrophages are critical for osteoblast maintenance and promote intramembranous and endochondral ossification during bone repair

Lena Batoon[1] (BBiomedSc), Susan Marie Millard[1] (PhD), Martin Eduard Wullschleger[2,3,6] (MD, PhD, FRACS), Corina Preda[4] (BSc/BComm, MBBS), Andy Chiu-Ku Wu[1] (PhD), Simranpreet Kaur[1,5] (MSc(Biotech)), Hsu-Wen Tseng[1] (PhD), David Arthur Hume[3,7] (PhD), Jean-Pierre Levesque[1,3] (PhD), Liza Jane Raggatt[1,3] (PhD) and Allison Robyn Pettit[1,3] (PhD).

1. Bones and Immunology Laboratory, Mater Research Institute-The University of Queensland, Translational Research Institute, Woolloongabba, Queensland, Australia 4102; **2.** Gold Coast University Hospital, Southport, Queensland, Australia, 4215; **3.** The University of Queensland, Faculty of Medicine, Herston, Queensland, Australia, 4092; **4.** Redcliffe Hospital, Queensland Health, Redcliffe, Queensland, Australia, 4020; **5.** The University of Queensland, Diamantina Institute, Translational Research Institute, Woolloongabba, Queensland, Australia 4102. **6.** Griffith University, School of Medicine, Southport, Queensland, Australia, 4215. **7.** The Roslin Institute and Royal (Dick) School of Veterinary Studies, University of Edinburgh, Roslin, Midlothian EH25 9PS, Scotland, UK

Corresponding Author: Allison R Pettit. Mater Research Institute-UQ, Translational Research Institute, 37 Kent Street, Woolloongabba, QLD, 4102. Phone: +617 3443 7575, Email: allison.pettit@mater.uq.edu.au

ABSTRACT

Osteal macrophages (osteomacs) contribute to bone homeostasis and regeneration. To further distinguish their functions from osteoclasts, which share many markers and growth factor requirements, we developed a rapid, enzyme-free osteomac enrichment protocol that permitted characterization of minimally manipulated osteomacs by flow cytometry. Osteomacs differ from osteoclasts in expression of Siglec1 (CD169). This distinction was confirmed using the CD169-diphtheria toxin (DT) receptor (DTR) knock-in model. DT treatment of naïve CD169-DTR mice resulted in selective and striking loss of osteomacs, whilst osteoclasts and trabecular bone area were unaffected. Consistent with a previously-reported trophic interaction, osteomac loss was accompanied by a concomitant and proportionately striking reduction in osteoblasts. The impact of $CD169^+$ macrophage depletion was assessed in two models of bone injury that heal *via* either intramembranous (tibial injury) or endochondral (internally-plated femoral fracture model) ossification. In both models, $CD169^+$ macrophage, including osteomac depletion compromised bone repair. Importantly, DT treatment in CD169-DTR mice did not affect osteoclast frequency in either model. In the femoral fracture model, the magnitude of callus formation correlated with the number of $F4/80^+$ macrophages that persisted within the callus. Overall these observations provide compelling support that $CD169^+$ osteomacs, independent of osteoclasts, provide vital pro-anabolic support to osteoblasts during both bone homeostasis and repair.

Keywords: osteomac, macrophage, bone regeneration, fracture repair, bone formation, osteoblast

INTRODUCTION

Fractures caused by either traumatic injury [1] or disease-induced skeletal fragility [2] impose a significant and growing [3] global health burden. Even when satisfactory bone repair is achieved using first-line orthopedic management, bone fracture causes loss of productivity, reduced functionality and increased mortality [4]. Fracture healing is protracted in approximately 10% of fracture cases which exhibit delayed union or non-union [5]. There is currently no broadly applicable acute fracture therapeutic, despite the demonstrated benefit of acute therapeutic intervention (INFUSE™) in open tibial fractures [6]. Improved understanding of fracture healing biology is needed to inform development of both pharmaceutical and/or biomaterial-based approaches to reinforce or recapitulate the true regenerative capacity of bone [7].

Fracture healing progresses sequentially through three interdependent and overlapping phases: inflammatory, anabolic and remodeling. Appropriate execution of events within the inflammatory phase is essential to successfully establishing bone healing [8-10] as it achieves assembly of a vascularized granulation tissue [11-14]. Mesenchymal condensation and bone anabolism initiate within the granulation tissue and the anabolic phase can progress *via* either endochondral and/or intramembranous ossification, with cell fate decisions influenced by the degree of fracture stability [15, 16]. The final remodeling phase involves coupled osteoclast-osteoblast activity to remove and remodel the temporary hard callus/woven bone into anatomically appropriate mature lamellar bone [15].

Identification and characterization of the resident macrophage population within the specialized tissues lining bone (osteal macrophages, osteomacs) [17] refocused attention on macrophage contributions to bone biology. Osteomacs have been shown to support osteoblast maturation, maintenance and function [17-26]. Multiple macrophage subsets contribute to fracture healing during both the inflammatory and anabolic phases, regardless of the ossification mechanism used

[20, 21, 24, 25, 27, 28]. Fracture-associated tissues contain recruited and resident macrophage subsets and their population dynamics vary both between intramembranous- and endochondral-mediated repair as well as longitudinally during progression of fracture healing [17, 27, 29]. Macrophages contribute to many of the processes needed for fracture repair induction, progression and resolution [29]. Moreover, they have important roles in immune responses to biomaterials. Macrophage depletion leads to inhibition of osteoinduction by bone grafting materials [30], further demonstrating their function in directing repair-associated osteogenesis. Therefore, macrophages represent an attractive therapeutic target to promote bone regeneration.

One limitation of previous studies investigating macrophage contributions to bone formation and repair has been collateral impacts on osteoclasts (specialized bone resorbing cells [31]) arising from *in vivo* 'macrophage' depletion approaches [17, 18, 24, 27, 28, 32]. Macrophages and osteoclasts share progenitors (myeloid lineage), growth factors (notably macrophage colony-stimulating factor, CSF1) and many molecular markers. Osteoclasts can be targeted with relatively high specificity without major impacts on macrophages (*e.g. via* osteoprotegerin, cathepsin K and calcitonin receptor based strategies) [33, 34]. However, commonly used 'macrophage' depletion approaches including clodronate liposome [35], lysozyme M driven-cre recombinase [36] and *Csf1r*-promoter or antibody based approaches [17, 25, 27, 37] also directly deplete osteoclasts [26, 30, 38]. As osteoclasts have established roles in long bone growth *via* endochondral ossification [39] and during fracture repair [15] that likely extend beyond their bone resorption function [40], their co-depletion somewhat confounds interpretation of the experimental outcomes. Despite strategies to reduce/compensate for the impact of macrophage depletion approaches on osteoclasts [18, 27] and the fact that osteoclast-specific targeting does not 'phenocopy' macrophage depletion model outcomes [27, 28, 41, 42], there is still ambiguity about the relative contribution of these cells to bone repair.

This study aimed to improve characterization of the macrophage subsets involved in bone biology and to separate macrophage from osteoclast contributions to *in vivo* bone homeostasis and repair. Based on literature and gene expression database interrogation, cluster of differentiation 169 (CD169) is a cell surface antigen reported to be restricted to mature resident macrophages [43], including those present in the bone marrow (BM) [44], and absent from osteoclast progenitors [45]. Herein, we confirm that CD169 expression distinguishes osteomacs from osteoclasts *in vitro* and *in vivo*, and utilize selective depletion of $CD169^{+}$ cells to achieve improved specificity in dissecting the functions of osteomacs in bone biology and repair.

MATERIALS AND METHODS

Experimental animals

Animal experiments were approved by The University of Queensland Health Sciences Ethics Committee and performed in accordance with the Australian Code of Practice for the Care and Use of Animals for Scientific Purposes. C57Bl/6 (wild type, WT) mice were obtained from Australian Resources Centre (Canning Vale, Western Australia, AU) and MacGreen *Csf1r* promoter-green fluorescent protein (GFP) reporter transgenic (B6N.Cg-Tg(Csf1r-EGFP)1Hume/J) mice [46], were maintained in-house. Heterozygous $CD169^{+/DTR}$ knock-in ($Siglec1^{tm1(HBEGF)Mtka}$) mice [47] were originally sourced from Riken Bio Resource Centre (Yokohama, Kanagawa, Japan) and contain the human diphtheria toxin (DT) receptor (DTR) knocked into the murine CD169 (*Siglec-1*) locus. Experimental $CD169^{+/DTR}$ mice were generated by F1 crosses of $CD169^{DTR/DTR}$ males with either WT or MacGreen (C57BL/6 background) females. As the $CD169^{DTR/DTR}$ x MacGreen F1 cross is benign with respect to mouse phenotype, all F1 $CD169^{+/DTR}$ have been referred to throughout as ‘CD169-DTR’. All mice were housed

under specific pathogen-free conditions in the Translational Research Institute Biological Resource Facility, fed standard chow with *ad libitum* water access and simulated diurnal cycle.

Enrichment of endosteal and periosteal cells

Both endosteal and periosteal enrichment methods were rapid enzyme free approaches, minimizing impact on macrophage phenotype. Femora harvested from female and male 4-week old MacGreen mice were used for enrichment of periosteal cells as previously described [29]. For enrichment of endosteal cells, extraneous muscle, connective tissue and periosteum were stripped from dissected femora and central BM was extracted by a coring approach using insertion of a 25G needle. This technique was evaluated as successful using standard histology (not shown). Endosteum was exposed by longitudinal and transverse cuts to the bone. Endosteal enriched cells were dislodged twice using a GentleMACS Dissociator tissue homogenizer with matching C tubes (Miltenyl Biotec, NSW, AU) on "m_speen_03" setting. Dislodged cells were washed twice, first with 4 mL and second with 3 mL 2% fetal calf serum (FCS) in phosphate buffered saline (PBS) and filtered using 40 um cell strainer.

Depletion of macrophages in naive CD169-DTR mouse model

Uninjured 8 to 10-week old male WT mice and CD169-DTR mice were randomly allocated to groups treated with vehicle (0.9% sodium chloride) or 10 μg/kg body weight of DT (MBL International Corporation, MA, USA) once daily *via* intra-peritoneal injection over 4 consecutive days. DT was prepared as previously described [48]. Bone tissues and BM were harvested 24 hours after the last injection.

$CD169^+$ cell depletion in a tibial bone injury model

Intramembranous-mediated bone repair mechanisms were assessed in 11 to 13-week old male mice that had a drill hole injury created in the left tibia as previously described [27, 49] but with a minor modification: defect was generated using a 0.85 mm drill bit attached to an electric drill

(RISystems, Davos Platz, CH). Animals were randomly allocated to vehicle or treatment groups. DT or vehicle treatment was initiated 1 day post-surgery and continued for 4 consecutive days as a daily injection. Tissues were collected 4 days post-injury (n = 4/group; inflammatory-anabolic transition) and 7 days post-injury (n = 6/group; peak anabolic phase) [27].

CD169^{+} cell depletion in the MouseFix-plated experimental femoral fracture model

A clinically relevant femoral fracture model using an internally fixed flexible plate (MouseFix, RISystems, Davos Platz, CH) [50] that heals through periosteal callus formation *via* endochondral ossification was used as previously described [28]. Experimental fractures were created in 11 to 14-week old male mice. Animals were randomly allocated to vehicle (n = 4) or DT (n = 7) groups. DT or vehicle treatment was initiated 1 day post-surgery and continued for 4 consecutive days as a daily injection. Tissues were collected 14 days post-surgery (peak early anabolic phase) [28].

Tissue collection

BM from the right femora was collected for flow cytometry by flushing with a 5 mL syringe mounted with 27G needle and 2 x 5 mL of 2% FCS in PBS. Left hind limbs were dissected, fixed, decalcified and processed for immunohistological analysis as previously described [27].

Flow cytometry

Cell suspensions were generated with 2% FCS in PBS and then incubated with the appropriate antibody cocktail for 40 minutes in the dark and on ice with agitation. The myeloid antibody cocktail was made in Fc (fragment crystallizable antibody region) block and contained anti-F4/80-Alexa647 (clone BM8; AbD Serotec, Kidlington, UK), anti-CD169-PE (clone 3D6.112; Biolegend, San Diego, CA, USA), anti-Lymphocyte antigen 6 complex locus G6D (Ly6G)-PE/Cy7 (clone 1A8; Biolegend) and anti-CD115-biotin (clone AFS98; Biolegend). In some experiments the myeloid cocktail also included anti-vascular cell adhesion molecule 1 (VCAM1)-

Pacific blue (clone 429; BD Biosciences, NJ, USA). The mesenchymal antibody cocktail contained anti-Ter119-biotin (clone Ter-119; Biolegend), anti-CD31-BV605 (clone 390; Biolegend), anti-Sca-1-PE/Cy7 (clone D7; Biolegend) and anti-CD51-PE (clone RMV-7; Biolegend). The antibody cocktail for detecting non-haematopoietic cells, including osteoblasts, in enriched osteal and bone marrow preparations contained F4/80 (clone BM8; AbD Serotec), CD45-APCCy5 (clone 30-F11; Biolegend), CD11b-BV605 (clone M1/70; Biolegend), and CD169 (clone 3D6.112; Biolegend). The antibody cocktail to detect osteoclast precursors consisted of anti-B220-FITC (clone RA3-6B2; Biolegend), anti-CD3-FITC (clone 145-2C11; Biolegend), anti-Ter119-biotin (clone Ter-119; Biolegend), anti-CD115-biotin (clone AFS98, Biolegend), anti-F4/80-Alexa647 (clone BM8; AbD Serotec), anti-Ly6C-APCFire750 (clone HK1.4; Biolegend), and anti-CD169-PE (clone 3D6.112; Biolegend) [51, 52]. Cells were then washed and incubated with the secondary antibody Strepavidin-PE-CF594 for 30 minutes. Cells were washed, resuspended in 300 μL 2% FCS in PBS. Specificity of staining was determined by comparison to unstained cells and appropriate isotype control cocktails. Five minutes prior to analysis 5 μg/mL 7-amino actinomycin D (Life Technologies, CA, USA) was added to each tube to allow exclusion of dead cells. Cells were examined *via* flow cytometry on a CyAn flow cytometer (Beckman Coulter, Brea, CA) and data were analyzed using FlowJo version 10 (Tree Star Data Analysis Software). Analyses were performed on live ($7AAD^-$) cells after cell aggregate exclusion. Low (lo) to intermediate (int) expression of either CD115 or GFP was used to segregate macrophages from monocytes due to lower expression of the *Csf1r* gene in macrophages. $CD169^+$ macrophages/osteomacs were gated as $F4/80^+Ly6G^-CD115^{lo\text{-}int}/GFP^{lo\text{-}int}CD169^+$ cells. Osteoblasts were gated as $Ter119^-CD45^-CD31^-Sca1^-CD51^+$ cells [53]. Conversion of gated population percent frequency to absolute cell number was achieved by a

standardized correction approach incorporating percent of live cells with total leucocyte count (Coulter AcT Diff Hematological Analyzer, Beckman and Coulter) per femoral BM.

Immunohistochemistry

Immunohistochemistry (IHC) was performed on deparaffinized and rehydrated sections with unconjugated primary antibodies against F4/80 (clone Cl:A3-1; rat anti-mouse; Novus Biological, CO, USA), collagen type 1 (Col1a1; polyclonal; rabbit anti-mouse; US Biological, Swampscott, MA, USA), osteocalcin (polyclonal; rabbit anti-mouse; Enzo Life Sciences, Farmingdale, NY, USA), or relevant isotype control antibodies (normal rat IgG2b (Biolegend, San Diego, CA, USA) and normal rabbit IgG (Santa Cruz Biotechnology, Inc., Santa Cruz, CA, USA). Briefly, sections were blocked for endogenous peroxidase activity and subsequently underwent antigen retrieval. For anti-osteocalcin and anti-Col1a1 staining this was achieved by treating tissues with 0.1% trypsin (Sigma-Aldrich, St Louis, MO) in PBS and for anti-F4/80 staining using microwave heat retrieval in 10 mM sodium citrate (pH 6.0). Non-specific antibody binding was blocked using appropriate serum cocktails for the secondary antibody or Background Sniper (Biocare Medical, Concord, CA). Primary antibodies were diluted in either Tris-buffered saline (osteocalcin and Col1a1) or Da Vinci Green Diluent (F4/80; Biocare Medical) and incubated with sections for 90 minutes. Sections were subsequently incubated with a biotinylated F(ab′)2 of species-matched secondary antibody: goat anti-rat or goat anti-rabbit (Santa Cruz Biotechnology) followed by HRP-conjugated streptavidin (Dako Agilent Pathology Solutions, Denmark). Diaminobenzidine was developed as per the manufacturer (Dako's) instructions and all sections were counterstained with Mayer's hematoxylin (Sigma-Aldrich). Specificity of staining was assessed in serial sections in the same staining run using matched concentrations of appropriate isotype control antibodies (for examples see Supplemental Figure 2A). Tartrate-

resistant acid phosphatase (TRAP) was performed as previously described [54] and Safranin-O staining done *via* standard histological protocol.

Staining was imaged using either a Vectra III Spectral scanner (PerkinElmer, Waltham, MA) and analyzed using inForm© Cell Analysis™ 2.2 software (PerkinElmer), or using Olympus BX50 microscope and imaged *via* Olympus CellSens standard software 7.1 (Olympus, Tokyo, JP). Anti-F4/80 and anti-galectin-3 dual immunofluorescence staining was performed as previously described [29].

Histomorphometric Methods

All sections were de-identified and assessed in a blinded manner. When analyses were based on area of staining or intensity of staining, automated software based approaches were used to reduce or eliminate human bias. Depending on the software used, either a single fully automatic algorithm or matched analysis threshold settings were applied to all samples within an experiment. $F4/80^+$ osteomac canopy and $osteocalcin^+$ osteoblast surface on the endosteal surface were quantified in uninjured tibia using adapted histomorphometry as described previously [17]. A length of 4-6 mm of bone surface in the mid-metaphyseal to mid-diaphyseal endosteal surface of the posterior aspect of the tibia was examined per section. Number of $F4/80^+$ cells were quantified by manual counting of positive cells in 0.09 ± 0.02 mm^2 of femoral periosteum.

For quantification of osteoclast frequency, area of TRAP staining, intensity of TRAP staining and trabecular bone area, tiled images (20x magnification) of metaphyseal trabecular bone from TRAP stained sections were collected. To quantify osteoclast frequency, percent surface of $TRAP^+$ staining per bone surface was quantified using ImageJ software (National Institutes of Health, NIH, Bethesda, MD, USA). Approximately 11 mm of bone surface length was examined in each section. For quantification of trabecular bone area and area of TRAP staining, the iterative training process within inForm© Cell Analysis™ 2.2 software (PerkinElmer) was used

to develop an algorithm which could segment images of the metaphyseal region into bone and BM, and detect magenta TRAP staining, respectively. Area of trabecular bone was expressed as a percentage of the total area of the region quantified which was on average approximately 1 ± 0.17 mm^2. The iterative training process within NIS-Elements Basic Research 3.22.09 software (Nikon Instruments Inc., Melville, NY, USA) was used to develop an algorithm which detected the intensity of the magenta-colored TRAP staining in tissue samples.

Tiled images of individual tibial injury sites (including inter-cortical injury zone and intra-medullary injury zone) were collected from anti-Col1a1 antibody-stained sections. inForm© Cell Analysis™ 2.2 software (PerkinElmer) was again used to develop an algorithm which segmented images of the injury site into regenerative tissue (woven bone, osteoblasts, condensing mesenchyme), scar tissue (fibrous connective tissue), bone (cortical and old bone) and other tissue (cortical bone fragments, BM, vascular sinuses). The algorithm utilized staining intensity and distribution of both diaminobenzidine chromogen (Col1a1) and hematoxylin (nuclei) to achieve image segmentation. Area of the regenerative tissue and scar tissue were subsequently expressed as a percentage of the injury zone.

For quantification of F4/80 staining in tibial injury samples, 20x magnification tiled images were collected and percent F4/80 staining area within the injury site was measured using ImageJ software (NIH). In femoral fracture samples, quantification of total callus area (within 1 mm distally and proximally from the osteotomy site) was performed on tiled images of the callus collected from Safranin-O stained sections using ImageJ.

In sections stained for F4/80, positive cells within the granulation tissue and woven bone regions of the callus were manually counted and expressed as number of $F4/80^+$ cells per mm^2 using ImageJ.

For all histology-based quantification methods described above, each data point represents the mean of analyses at 3 sectional depths/sample that were at least 50 μm apart.

Serum TRAP-5b Immunoassay

Blood was collected at time of euthanasia of DT or vehicle-treated CD169-DTR and WT mice *via* cardiac puncture. Blood samples were allowed to clot at room temperature for 15 minutes and centrifuged at 3000 g for 10 minutes at 24ºC. Supernatants were collected. Serum TRACP-5b activity was assayed using MouseTRAP Assay TRACP-5b ELISA kit (Immunodiagnostic Systems, Boldon, Tyne and Wear, UK) as per the manufacturer's instructions.

Statistical analyses

Statistically significant differences were determined where appropriate using either a one-way ANOVA with Tukey's post-test or two-tailed unpaired t-test in PRISM 5 (GraphPad Software, La Jolla, CA). A value of $p < 0.05$ was considered statistically significant.

RESULTS

Macrophages within enriched endosteal and periosteal cell preparations express the mature macrophage marker CD169

Macrophage characteristics can be significantly altered by *ex vivo* isolation and manipulation [55]. Therefore we developed a rapid, digestion-free technique to enrich for endosteal and periosteal osteomacs using MacGreen mice. The approach was verified by examining enrichment of osteoblasts (gated as per details in Materials and Methods and Supplemental Figure 1A) which should be abundant in periosteum and endosteum. Endosteal and periosteal preparations had a 2-fold and 22-fold higher frequency of $Ter119^{-}CD45^{-}CD31^{-}Sca1^{-}CD51^{+}$ osteoblasts [53] respectively compared to central BM (Figure 1A). By inference, these preparations should also be enriched for osteomacs over other central marrow resident macrophage populations [56].

The mouse transcriptional atlas data available at www.biogps.org [57] includes multiple macrophage, osteoclast and osteoblast profiles from *ex vivo* cultures produced in our laboratories. This data set confirmed the highly restricted expression of *Siglec1*, encoding CD169, in mouse macrophages, with minimal expression in osteoclast cultures (which contain 'contaminating' mononuclear cells including macrophages) and no expression in osteoblasts (data not shown). Assessment of *siglec1* mRNA expression in primary murine osteoblasts, osteoclasts, bone marrow-derived macrophages and bone marrow mesenchymal stromal cells confirmed expression of *siglec1* is restricted to macrophages within these relevant cell populations (Supplemental Figure 1B). Monoclonal anti-mouse CD169 antibodies are not indicated for paraffin embedded tissues and were not useful for determination of CD169 expression *in situ*. Therefore we investigated CD169 expression by flow cytometry in macrophages within enriched osteal tissue preparations, which by inference contain a high proportion of osteomacs. Resident macrophages, gated as $F4/80^{+}Ly6G^{-}VCAM1^{+}GFP^{low\text{-}mid}$ (Figure 1B, left and middle panels), were present in both the endosteal and periosteal enriched cell preparations and approximately 40% of these expressed CD169 (Figure 1B, right panel, and C). Non-hematopoietic cells (Figure 1D, includes mesenchymal and endothelial cells) as well as hematopoietic osteoclast precursors/progenitors, gated as per previously published and characterized [51, 52] (Figure 1E), within these cell preparations expressed minimal to no CD169.

$CD169^{+}$ osteomacs are required for osteoblast maintenance *in vivo*

To confirm CD169 expression by osteomacs *in vivo* and secondary impacts of $CD169^{+}$ macrophage depletion on osteoblasts, we utilized the CD169-DTR knock-in mouse model. DT was delivered as previously described [48] and cells and tissue collected as indicated in the schematic in Figure 2A. To control for CD169 haploinsufficiency in CD169-DTR mice (*i.e.* knock-in model), vehicle-treated WT and CD169-DTR mouse control groups were included. To

control for potential non-DTR transgene toxicity of DT, WT mice were treated with the same DT regimen.

To gauge the depletion efficiency of the DT treatment protocol, the impact on bone marrow F480^{+}Ly6G^{-} cell number, which includes macrophages and monocytes is shown in Figure 2B. This broader myeloid gating was used as a first pass assessment to clarify whether any population reductions demonstrated using CD169 expression dependent gating were biased by reduced CD169 expression as a consequence of *Siglec1* haploinsufficiency in CD169-DTR mice. DT treatment of WT mice did not impact on F4/80^{+}Ly6G^{-} cell frequency supporting minimal off target toxicity of the DT treatment. Interestingly, saline-treated CD169-DTR mice had significantly lower F4/80^{+}Ly6G^{-} frequency compare to saline WT, suggesting there was an impact of *Siglec1* haploinsufficiency on BM monocyte/macrophage frequency. When compared to all other groups, F4/80^{+}Ly6G^{-} cells were significantly depleted in DT treated CD169-DTR mice (Figure 2B). Within the F4/80^{+}Ly6G^{-} gate, the relative proportion of CD11b^{+}CD115/GFP^{high} monocytes increased 4-fold (16.4 ± 2.3% versus 68.9 ± 8.9% in vehicle versus DT treated CD169-DTR mice respectively), an anticipated outcome based on lack of CD169 expression by monocytes. Overall, DT treatment in CD169-DTR mice induced selective depletion of F4/80^{+}Ly6G^{-} mature myeloid cells while preserving BM monocytes, further exemplifying the specificity of this macrophage depletion model.

There was profound loss of CD169^{+} BM resident macrophages (F4/80^{+}Ly6G^{-}CD115^{lo}CD169^{+}) in DT-treated CD169-DTR mice compared to all control groups (Figure 2C, $p < 0.001$). As this mirrored the observations in Figure 2B where cell population gating was not dependent on CD169, the observed depletion is unlikely to be contributed to by reduced CD169 immuno-reactivity. Similar to F4/80^{+}Ly6G^{-} cells, *Siglec1* haploinsufficiency was associated with a significant reduction in CD169^{+} BM resident macrophage number (Figure 2C, WT-vehicle versus

CD169-DTR-vehicle mice). There was no off target toxicity of DT on BM CD169$^+$ resident macrophage number (Figure 2C, WT-vehicle compared to WT-DT treated).

The impact of four sequential doses of DT was examined *in situ* using IHC in hind limb sagittal sections from the same experimental cohorts of WT and CD169-DTR mice used in Figure 2B-C. Anti-F4/80 antibody staining in combination with anatomical location was used to distinguish osteomacs [17]. In all control groups, F4/80$^+$ macrophages were abundant in the central marrow (Figure 2D(i-iii)). F4/80$^+$ endosteal osteomacs were observed on resting bone surfaces (not shown) and forming canopy-like structures over sites of active bone modelling (Figure 2D(i-iii), red arrows). Serial sections stained with anti-osteocalcin confirmed that these canopy osteomacs were adjacent to cuboidal osteocalcin$^+$ osteoblasts lining the bone surface (Figure 2D(v-vii), black arrows), as previously reported [17]. DT treatment in CD169-DTR mice greatly reduced the number of F4/80$^+$ central marrow macrophages (Figure 2D(iv)). Importantly, F4/80$^+$ osteomacs and osteocalcin$^+$ osteoblasts were rarely observed on endosteal bone surfaces in DT treated CD169-DTR mice (Figure 2D(iv and viii)). Loss of periosteal F4/80$^+$ osteomacs was evident in both metaphyseal (not shown) and diaphyseal regions (Figure 3A-D). Osteomac loss was evident after one dose of DT (Figure 3A) whilst the endosteal osteoblast surface was not appreciably impacted until 3 doses of DT had been administered (Figure 3D).

These observations were verified by histomorphometry [17]. In the endosteum, DT treatment alone and *Siglec1* haploinsufficiency both resulted in small off-target impacts on the amount of endosteal bone surface that had associated osteomac coverage (Figure 3E). *Siglec1* haploinsufficiency was also associated with a 24% reduction in endosteal osteoblast surface (Figure 3F). Strikingly, DT treatment in CD169-DTR mice produced almost complete loss of F4/80$^+$ endosteal osteomacs (Figure 3E, $p < 0.001$) which was accompanied by a 92% reduction of osteocalcin$^+$ osteoblast-covered bone surface (Figure 3F, $p < 0.001$). No difference in

periosteal F4/80$^+$ macrophage number was observed between the control groups (Figure 3G), indicating that *Siglec1* haploinsufficiency and toxin off-target impacts are negligible in this tissue. Whereas profound loss of F4/80$^+$ periosteal osteomacs occurred in DT-treated CD169-DTR mice compared to all control groups (Figure 3G, $p < 0.001$).

TRAP$^+$ multinucleated osteoclasts were abundant in tibial metaphyseal bone of WT and CD169-DTR mice irrespective of treatment (Figure 4A-D). As expected based upon the lack of CD169 in BM osteoclast precursors (Figure 1D) and *Siglec1* mRNA in osteoclasts (Supplementary Figure 1B), there was no difference between the percent area of TRAP$^+$ surface/bone surface (Figure 4E), percent area of TRAP staining within the metaphyseal region (Figure 4F) and TRAP staining intensity (Figure 4G) between DT-treated CD169-DTR mice and the control groups. While serum TRAP-5b activity was unexpectedly increased in DT-treated CD169-DTR mice (Figure 4H) compared to all control groups, there was no difference in trabecular bone area within the metaphyseal region (Figure 4I), suggesting that the treatment regimen did not alter osteoclast resorption activity. Consequently, assessment of total bone volume, bone mineral density and/or dynamic histomorphometry was not undertaken as *in situ* data indicated that the DT protocol used did not cause bone loss. Moreover, while the DT treatment regimen did result in dramatic loss of osteoblast surface, this was only evident within the final 24 hr of the experimental time course and therefore was unlikely to have had sufficient time to impact bone volume. Within the bone and marrow environment, the data support selective depletion of macrophages, including osteomacs in the CD169-DTR model. Of specific relevance, bone marrow monocytes and osteoclasts were not affected.

CD169$^+$ osteomacs are required for normal bone repair *via* intramembranous ossification

To assess the functional contribution of CD169$^+$ osteomacs to bone repair we used a previously validated tibial injury model that primarily heals *via* intramembranous ossification, forming

woven bone that bridges the injury site [27, 49]. To determine the impact of $CD169^+$ macrophage loss during granulation tissue formation, DT or vehicle delivery was initiated 1 day post injury in CD169-DTR mice and repeated for the following 2 days. Tissues were harvested at day 4 post-injury (Figure 5A). This treatment regimen resulted in a significant reduction in $F4/80^+Ly6G^-$ cells (Figure 5B) and $CD169^+$ macrophages (Figure 5C) in the contralateral femur BM of DT-treated CD169-DTR mice, confirming efficacy of the DT regimen within each experimental animal. The percent area of $F4/80^+$ staining within the injury site was reduced in DT-treated compared to vehicle-treated CD169-DTR mice (Figure 5D). In vehicle-treated CD169-DTR mice, $F4/80^+$ macrophages were: 1) abundant in adjacent BM; 2) dispersed throughout the injury site associated granulation tissue; and 3) accumulated at the peripheral injury zone (Figure 5E). In the DT-treated CD169-DTR mice $F4/80^+$ macrophages were: 1) greatly reduced in the adjacent BM; 2) rare within the granulation tissue; and 3) present, but at reduced frequency, in the peripheral injury zone (Figure 5F).

To examine impact of $CD169^+$ macrophage depletion on woven bone deposition, DT or vehicle delivery was again initiated 1 day post injury in WT and CD169-DTR mice and sustained for 4 days (Figure 6A). Tissues were harvested 7 days post injury, which represents the peak anabolic phase with full bridging of the defect site with woven bone in WT mice [27]. At day 7 post injury, despite 3 days respite from DT treatment, substantial depletion of the contralateral limb BM $CD169^+$ macrophages (Figure 6B, $p < 0.001$) and a parallel reduction of the total $F4/80^+Ly6G^-$ macrophage/monocyte pool (Figure 6C, $p < 0.001$) were maintained in DT-treated CD169-DTR mice.

DT treatment impacts on macrophages and $Col1a1^+$ woven bone deposition within the injury site were assessed *in situ* (Figure 6D-I) using the same experiment cohort represented in Figure 6B-C. In vehicle-treated CD169-DTR mice, $F4/80^+$ macrophages were abundant within adjacent BM

(Figure 6D, asterisk) and intercalated within the injury site forming canopy-like structures over Col1a1^{+} woven bone surfaces (Figure 6E-F). Although sustained profound BM CD169^{+} macrophage depletion was demonstrated in the contralateral limb in DT-treated CD169-DTR mice (Figure 6B and C), F4/80^{+} macrophages were detected within the injury site (Figure 6G), but the percent area of F4/80 staining, a surrogate of cell number [27], was significantly reduced compared to controls (Figure 6J). In control mice the injury-associated F4/80^{+} macrophages displayed elongated osteomac morphology and were distributed within the woven bone bridge (Figure 6D-F). Double immunofluorescence staining indicated these macrophages were a mix of galectin-3^{+} and galectin-3$^{dim/-}$ cells (Figure 7), as previously reported [27]. In contrast, macrophages within DT-treated CD169-DTR mice were predominantly of ramified inflammatory macrophage morphology (Figure 6H) but were negative for the inflammatory marker galectin-3 (Figure 7) [58, 59].

Col1a1 deposition in the injury site of DT-treated CD169-DTR mice was reduced compared to controls (Figure 6F and I), and when present, had mixed morphological characteristics with some areas resembling woven bone while others resembled fibrotic tissue (Figure 6I, Supplemental Figure 2B). A reduction in woven bone and increase in fibrotic tissue was confirmed in DT-treated CD169-DTR mice by algorithm based segmentation of the injury site into regenerative tissue and fibrotic tissue (Supplemental Figure 2B and Figure 6K). DT treatment in wild type mice (ie. off-target DT toxicity) had no impact on F4/80^{+} macrophage number within the injury site and Col1a1 deposition (Supplemental Figure 3A-C). Quantitative (Figure 6L) and qualitative (Supplemental Figure 4A-B) examination of TRAP staining in metaphyseal trabecular bone of the injured limb indicated no difference in osteoclast frequency between the groups. TRAP^{+} osteoclasts were also readily detected in association with the injury site irrespective of treatment, but were not quantified as outcomes would be confounded by differences in the bone

422 regenerative response in DT-treated versus control CD169-DTR mice (Supplemental Figure 3C-
423 F).

424 **CD169$^+$ osteomacs are required for optimal fracture healing *via* endochondral ossification**

425 The requirement for CD169$^+$ osteomacs/macrophages in callus formation *via* endochondral
426 ossification was tested using an internally plated (MouseFix) femoral fracture model [28, 50, 60-
427 63]. Femoral fractures were generated in WT and CD169-DTR mice and DT or vehicle were
428 administrated for 4 days, initiating 1 day post-surgery, and tissue was collected at day 14 (Figure
429 8A).

430 Callus formation progression in vehicle-treated CD169-DTR mice was as expected for tissues
431 collected at the peak of the early anabolic phase, largely consisting of a soft cartilaginous callus
432 that was being progressively remodeled and replaced by woven bone (hard callus, Figure 8D).
433 DT treatment in wild type mice had no impact on F4/80$^+$ macrophage number within the
434 granulation tissue and woven bone, and on callus size (Supplementary Figure 3D-E) indicating
435 minimal fracture repair toxicity of the employed DT regimen. Robust depletion of F4/80$^+$Ly6G$^-$
436 myeloid cells (Figure 8B) and CD169$^+$ BM macrophages (Figure 8C) was sustained in the
437 contralateral limb of DT-treated compared to vehicle-treated CD169-DTR mice, even though
438 tissues were collected 10 days after the last DT dose. Surprisingly, F4/80$^+$ cells were detected
439 within the injured limb BM *via in situ* IHC (data not shown) indicating potential variation in
440 macrophage recovery dynamics in the injured limb. F4/80$^+$ macrophages within the periosteal-
441 like tissue encapsulating the maturing callus were also observed in all mice (Figure 8F-G).
442 However, callus formation in DT-treated CD169-DTR mice was stunted as shown by a
443 significant decrease in overall size (Figure 8D-H). In all vehicle-treated CD169-DTR mice,
444 F4/80$^+$ osteomacs were abundant in woven bone forming at the periphery of the maturing soft
445 callus (Figure 8D and F). Woven bone was absent from calluses in 3 out of 7 DT-treated CD169-

DTR mice (data not shown). There was a significant reduction in the number of $F4/80^+$ cells/mm^2 within total callus granulation tissue and woven bone of DT-treated versus vehicle-treated CD169-DTR mice (Figure 8I). Overall, $CD169^+$ osteomac/macrophage depletion had significantly impaired bone healing *via* periosteal callus formation (Figure 8H, $p < 0.01$). Within the $CD169^+$ macrophage-depleted experimental group, variation in the magnitude of fracture repair was observed (Figure 8H, range: 0 – 2 mm^2 total callus area). Some animals exhibited minimal-small callus formation in which granulation tissue still predominated (Figure 8G) whereas others had calluses that morphologically resembled control calluses but were appreciably smaller (not shown). These differences likely reflected biological variation in $CD169^+$ macrophage depletion and/or recovery kinetics. Interestingly, a positive correlation between $F4/80^+$ macrophage frequency in the callus and total callus size was observed ($r = 0.9$, $p \leq 0.001$, Figure 8J) when all mice were examined, recapitulating prior observations using alternative macrophage depletion approaches [28].

DISCUSSION

There is increasing recognition of the importance of macrophages in tissue repair processes [64], particularly in organs such as liver [65] and bone [28] that undergo a regenerative response. When added to macrophage contributions to innate immunity, particularly foreign body reactions [66, 67], carefully considered and targeted manipulation of macrophage function will be needed when developing biomaterial approaches for tissue repair. However, controversy persists relating to the role of macrophages in bone formation and regeneration. This in part originated from the historical misconception that macrophages within the bone microenvironment primarily represent a transient maturation stage in osteoclastogenesis, and this has been perpetuated by limitations associated with available 'macrophage' depletion models. These limitations include: 1)

unsatisfactory specificity of targeting macrophages versus other myeloid lineage cells, particularly osteoclasts; 2) variation in macrophage depletion magnitude depending on delivery route and/or delivered regimen of depletion triggering mechanism; and 3) that systemic depletion is generally induced. Herein we developed a minimal manipulation strategy to achieve osteal tissue enrichment and subsequently used a multiplexed flow cytometry approach to characterize osteomac cell-surface phenotype. Both endosteal and periosteal osteomacs expressed the highly restricted mature macrophage marker CD169. Of particular benefit, we provided *in vivo* evidence that expression of CD169 permitted positive selection/depletion of macrophages with exclusion/preservation of osteoclasts. Specifically we demonstrated that: *in vitro* generated osteoclast cultures had negligible expression of *siglec1* mRNA, confirmed that osteoclast precursors do not express CD169 [45] and showed that CD169-targeted cell depletion had no negative effects on mature osteoclast number, size, TRAP expression intensity or bone resorption activity. In contrast, CD169-targeted cell depletion resulted in rapid and profound loss of both periosteal and endosteal osteomacs. Importantly the latter was accompanied by a striking reduction in endosteal osteoblasts.

While we have demonstrated the potential benefits of the CD169-DTR model as an experimental tool for studying osteomac/macrophage contributions to bone biology and pathology, this model still has limitations. Although CD169 expression is highly specific to macrophages, it is not osteomac restricted. In lymphoid organs CD169 is expressed by specific subpopulations of resident macrophages with reported roles in immune regulation and tolerance [68]. Some resident macrophages within colon, kidney and liver have also been demonstrated to express CD169 [68]. Within bone and BM, use of the CD169-DTR model facilitated identification of hematopoietic stem cell (HSC) niche [44] and erythroid island [48, 69] macrophages. Indeed, $CD169^{+}$ macrophage depletion impacts on the HSC niche may have delayed knock-on effects on

494 osteoclasts and other central marrow macrophages, irrespective of their CD169 expression status,
495 *via* disruption of precursor supply [26, 44]. While this caveat had minimal impact on the
496 experiments reported herein (i.e. monocyte pool was unperturbed), it could become a
497 confounding factor in long time course experiments. On the flip side, not all BM, endosteal or
498 periosteal macrophages ($F4/80^{+}Ly6G^{neg}GFP/CD115^{lo}VCAM\text{-}1^{+}$) expressed CD169 and
499 consequently were not depleted in the CD169-DTR model. While this confirms refined targeting
500 precision within the multidimensional macrophage pool, compensatory mechanisms likely come
501 into play, especially given macrophage plasticity and potential rapid maturation from recruited
502 monocytes that were also maintained in this model. Available anti-mouse CD169 antibodies are
503 not indicated for use in paraffin embedded tissues and we were unable to develop a validated
504 anti-CD169 immunohistochemistry protocol. Reliance on anti-F4/80 immunohistochemistry to
505 assess the impact of $CD169^{+}$ cell depletion did somewhat reduce analysis precision. Overall, we
506 have demonstrated the benefits of using CD169-DTR mice for dissection of bone biology and
507 pathological mechanisms, however, as for all macrophage depletion model, careful experimental
508 design and interpretation is still warranted.
509 Even though hind limb osteoclast number, size, TRAP staining intensity characteristics and
510 trabecular bone volume were unaltered, increased serum TRAP activity was observed following
511 $CD169^{+}$ macrophage depletion. Based on the collective data, it is unlikely that this observation
512 reflects an actual increase in osteoclast activity, although we cannot rule out that osteoclast
513 activity was increased at other skeletal sites not examined herein. An alternative explanation is
514 that $CD169^{+}$ macrophage phagocytic function within the bone microenvironment is responsible
515 for clearance of excess TRAP produced during resorption events. Demonstration of close
516 association of $F4/80^{+}$ osteomacs to $TRAP^{+}$ osteoclast at bone resorption sites, including within
517 basic multicellular units [70], as well as presence of TRAP activity within phagocytic vesicles

518 with F4/80^{+} macrophages [27] support this interpretation. While it is well known that
519 macrophages, through production of inflammatory cytokines, can drive osteolytic responses in
520 pathology [66], further investigation is required to determine whether macrophages, particularly
521 osteomacs, have specific secondary support roles during bone resorption associated with bone
522 growth and homeostasis.

523 The impact of CD169^{+} osteomac depletion on the *in vivo* maintenance of endosteal osteoblasts
524 irrefutably confirmed conclusions using less refined macrophage targeting strategies regarding
525 the importance of osteomacs in supporting bone formation [17, 18, 25, 27]. Osteoblast loss was
526 subsequent to osteomac depletion and is unlikely to be a specific bystander effect of induced-
527 osteomac death, as each of the experimental models achieves this outcome through highly varied
528 death mechanisms (*e.g.* Fas-mediated apoptosis in Mafia mice, inhibition of mitochondrial
529 ADP/ATP translocase by clodronate loaded liposomes versus inhibition of protein synthesis
530 induced by DT). Hematopoietic stem cell mobilizing regimens of granulocyte colony stimulating
531 factor also caused osteomac loss and subsequent osteoblast loss, with osteomac egress from BM
532 implicated as the mechanism rather than osteomac death [26]. The magnitude of the osteoblast
533 loss suggests that osteomacs either produce a required survival factor or that they support
534 osteoblast maintenance through multiple mechanisms that culminate in essential symbiosis.
535 Identification of these mechanisms is the next frontier for osteomac research and will be
536 facilitated by the technical advances reported herein.

537 CD169^{+} osteomac depletion impaired bone regeneration, irrespective of the ossification
538 mechanism. The impact of CD169^{+} osteomac depletion initiated at the time of surgery on bone
539 regeneration was not as pronounced as broad spectrum macrophage depletion initiated with the
540 same timing, instead resembling outcomes of delayed broad spectrum depletion [27, 28].
541 Specifically, in Mafia mice callus formation was completely abolished after 'macrophage'

depletion initiated at the time of fracture. Whereas in DT-treated CD169-DTR mice, callus formation still initiated in all but one mouse, however these calluses were significantly smaller. Differences in the degree of healing between the depletion models could be interpreted in two ways. First, that $CD169^+$ osteomacs have a lesser role in the inflammatory phase of bone repair. Second, their role in bone repair initiation can be at least partially compensated for by $CD169^-$ macrophages but that $CD169^+$ macrophages become more critical as healing progresses toward the anabolic phase. These nuances will be difficult, but potentially important to dissect experimentally. They do not detract from the overall conclusion being that macrophages including $CD169^+$ osteomacs play key roles in successful progression of bone healing.

An intriguing observation was that in the tibial defect model, depletion of $CD169^+$ osteomacs/macrophages changed the balance between bone regeneration versus fibrosis, favoring the latter. In normally healing tibial injuries, a mix of galectin-3^+ and galectin-3^- osteomacs were abundant within the injury site where they were associated with osteoblasts and woven bone surfaces particularly in the inter-cortical region. Galectin-3 is highly expressed on pro-healing alternatively activated macrophages [58, 59]. Moreover, $F4/80^+$galectin-3^+ macrophages are present at the metaphyseal corticalization zone in growing mice, which is a site of complex bone dynamics regulating cortical bone lengthening [29]. When bone repair was compromised due to $CD169^+$ osteomac/macrophage depletion, galectin-3^- macrophages predominated in the injury site. This suggests that depletion of $CD169^+$ macrophages has specifically reduced the number of pro-regenerative macrophages within the injury site which conforms to the herein observed increase in fibrotic scar tissues within tibial injury sites. The observations highlight that the appropriate functional subset of macrophages is required to achieve the desired regenerative outcomes which will be an important consideration for therapeutic and/or biomaterial approaches designed to enhance bone repair [66]. More in-depth understanding of phenotype and molecular

profiles of pro-bone healing macrophages and what environmental inputs promote the functional maturation is needed to better inform design of bone healing interventions.

In conclusion, we have provided direct evidence that $CD169^{+}$ osteomacs, independent of osteoclasts, provide vital pro-anabolic support to osteoblasts during bone homeostasis and repair. The CD169-DTR model provides a unique experimental tool for differentiating the functional contributions of osteomacs and osteoclasts in bone biology and the development of therapeutic and biomaterial approaches to enhance bone repair. This model will facilitate further investigations into the role of osteomacs during the remodeling phase of bone repair and whether macrophages contribute to osteoclast biology. Finally, perturbations in osteomac/macrophage functional contributions and resultant changes to the reparative inflammatory process should be considered as a potential primary underlying mechanism for delayed healing and non-union outcomes in bone fractures.

Acknowledgments: This work was supported by the Mater Foundation, an Arthritis Australia Project Grant to ARP, an Australian and New Zealand Bone and Mineral Society Gap Fellowship to ARP, and a National Health and Medical Research council Research Fellowship to JPL (APP1044091). The Translational Research Institute (TRI) Microscopy, Histology and Flow cytometry Core Facilities contributed technical expertise and the TRI Biological Research Facility contributed to animal husbandry and monitoring. Professor John Prins provided constructive advice on study design.

Authors Roles: LB, SM and LR planned and undertook experiments, performed data analysis. AW, SK and HT assisted in experimental execution. MW and PC performed mouse fix surgery.

589 DH and JPL provided scholarly advice and reagents. AP coordinated research. LB, LR and AP
590 wrote the manuscript and all other authors edited and approved manuscript.
591

References

[1] Mathew G, Hanson B. Global burden of trauma: Need for effective fracture therapies. Indian J Orthop. 2009;43:111-6.

[2] Hernlund E, Svedbom A, Ivergard M, Compston J, Cooper C, Stenmark J, et al. Osteoporosis in the European Union: medical management, epidemiology and economic burden. A report prepared in collaboration with the International Osteoporosis Foundation (IOF) and the European Federation of Pharmaceutical Industry Associations (EFPIA). Archives of Osteoporosis. 2013;8:013-0136.

[3] Odén A, McCloskey EV, Kanis JA, Harvey NC, Johansson H. Burden of high fracture probability worldwide: secular increases 2010–2040. Osteoporos Int. 2015;26:2243-8.

[4] Heckman JD, Sarasohn-Kahn J. The economics of treating tibia fractures. The cost of delayed unions. Bulletin of the Hospital for Joint Disease. 1997;56:63-72.

[5] Gómez-Barrena E, Rosset P, Lozano D, Stanovici J, Ermthaller C, Gerbhard F. Bone fracture healing: Cell therapy in delayed unions and nonunions. Bone. 2015;70:93-101.

[6] McKay WF, Peckham SM, Badura JM. A comprehensive clinical review of recombinant human bone morphogenetic protein-2 (INFUSE Bone Graft). International orthopaedics. 2007;31:729-34.

[7] Marsell R, Einhorn TA. The biology of fracture healing. Injury. 2011;42:551-5.

[8] Loi F, Cordova LA, Pajarinen J, Lin TH, Yao Z, Goodman SB. Inflammation, fracture and bone repair. Bone. 2016;86:119-30.

[9] Mountziaris PM, Mikos AG. Modulation of the inflammatory response for enhanced bone tissue regeneration. Tissue engineering Part B, Reviews. 2008;14:179-86.

[10] Waters RV, Gamradt SC, Asnis P, Vickery BH, Avnur Z, Hill E, et al. Systemic corticosteroids inhibit bone healing in a rabbit ulnar osteotomy model. Acta orthopaedica Scandinavica. 2000;71:316-21.

[11] Bourque WT, Gross M, Hall BK. Expression of four growth factors during fracture repair. IJDB. 1993;37:573-9.

[12] Einhorn TA, Majeska RJ, Rush EB, Levine PM, Horowitz MC. The expression of cytokine activity by fracture callus. J Bone Miner Res. 1995;10:1272-81.

[13] Schmidt-Bleek K, Schell H, Lienau J, Schulz N, Hoff P, Pfaff M, et al. Initial immune reaction and angiogenesis in bone healing. Journal of Tissue Engineering and Regenerative Medicine. 2014;8:120-30.

[14] Street J, Bao M, deGuzman L, Bunting S, Peale FV, Ferrara N, et al. Vascular Endothelial Growth Factor Stimulates Bone Repair by Promoting Angiogenesis and Bone Turnover. Proc Natl Acad Sci USA. 2002;99:9656-61.

[15] Gerstenfeld LC, Cullinane DM, Barnes GL, Graves DT, Einhorn TA. Fracture healing as a post-natal developmental process: Molecular, spatial, and temporal aspects of its regulation. J Cell Biochem. 2003;88:873-84.

[16] Gröngröft I, Heil P, Matthys R, Lezuo P, Tami A, Perren S, et al. Fixation compliance in a mouse osteotomy model induces two different processes of bone healing but does not lead to delayed union. J Biomech. 2009;42:2089-96.

[17] Chang MK, Raggatt LJ, Alexander KA, Kuliwaba JS, Fazzalari NL, Schroder K, et al. Osteal tissue macrophages are intercalated throughout human and mouse bone lining tissues and regulate osteoblast function in vitro and in vivo. Journal of immunology (Baltimore, Md : 1950). 2008;181:1232-44.

[18] Cho SW, Soki FN, Koh AJ, Eber MR, Entezami P, Park SI, et al. Osteal macrophages support physiologic skeletal remodeling and anabolic actions of parathyroid hormone in bone. Proc Natl Acad Sci USA. 2014;111:1545-50.

[19] Fernandes TJ, Hodge JM, Singh PP, Eeles DG, Collier FM, Holten I, et al. Cord Blood-Derived Macrophage-Lineage Cells Rapidly Stimulate Osteoblastic Maturation in Mesenchymal Stem Cells in a Glycoprotein-130 Dependent Manner. PLoS ONE 2013;8:e73266.

[20] Guihard P, Boutet M-A, Brounais-Le Royer B, Gamblin A-L, Amiaud J, Renaud A, et al. Oncostatin M, an Inflammatory Cytokine Produced by Macrophages, Supports Intramembranous Bone Healing in a Mouse Model of Tibia Injury. Am J Pathol. 2015;185:765-75.

[21] Guihard P, Danger Y, Brounais B, David E, Brion R, Delecrin J, et al. Induction of Osteogenesis in Mesenchymal Stem Cells by Activated Monocytes/Macrophages Depends on Oncostatin M Signaling. STEM CELLS. 2012;30:762-72.

[22] Nicolaidou V, Wong MM, Redpath AN, Ersek A, Baban DF, Williams LM, et al. Monocytes induce STAT3 activation in human mesenchymal stem cells to promote osteoblast formation. PLoS ONE 2012;7:e39871.

[23] Pirraco RP, Reis RL, Marques AP. Effect of monocytes/macrophages on the early osteogenic differentiation of hBMSCs. Journal of Tissue Engineering and Regenerative Medicine. 2013;7:392-400.

[24] Schlundt C, El Khassawna T, Serra A, Dienelt A, Wendler S, Schell H, et al. Macrophages in bone fracture healing: Their essential role in endochondral ossification. Bone. 2015.

[25] Vi L, Baht GS, Whetstone H, Ng A, Wei Q, Poon R, et al. Macrophages promote osteoblastic differentiation in-vivo: implications in fracture repair and bone homeostasis. J Bone Miner Res. 2014;8.

660 [26] Winkler IG, Sims NA, Pettit AR, Barbier V, Nowlan B, Helwani F, et al. Bone marrow
661 macrophages maintain hematopoietic stem cell (HSC) niches and their depletion mobilizes HSCs.
662 Blood. 2010;116:4815-28.
663 [27] Alexander KA, Chang MK, Maylin ER, Kohler T, Müller R, Wu AC, et al. Osteal
664 macrophages promote in vivo intramembranous bone healing in a mouse tibial injury model. J
665 Bone Miner Res. 2011;26:1517-32.
666 [28] Raggatt LJ, Wullschleger ME, Alexander KA, Wu ACK, Millard SM, Kaur S, et al. Fracture
667 healing via periosteal callus formation requires macrophages for both initiation and progression
668 of early endochondral ossification. Am J Pathol. 2014;184:3192-204.
669 [29] Alexander KA, Raggatt LJ, Millard S, Batoon L, Wu AK, Chang MK, et al. Resting and
670 injury-induced inflamed periosteum contain multiple macrophage subsets that are located at sites
671 of bone growth and regeneration. Immunology and Cell Biology 2016.
672 [30] Davison NL, Gamblin A-L, Layrolle P, Yuan H, de Bruijn JD, Barrère-de Groot F.
673 Liposomal clodronate inhibition of osteoclastogenesis and osteoinduction by submicrostructured
674 beta-tricalcium phosphate. Biomaterials. 2014;35:5088-97.
675 [31] Väänänen HK, Zhao H, Mulari M, Halleen JM. The cell biology of osteoclast function.
676 Journal of Cell Science 2000;113:377-81.
677 [32] Xing Z, Lu C, Hu D, Miclau T, Marcucio RS. Rejuvenation of the inflammatory system
678 stimulates fracture repair in aged mice. Journal of Orthopaedic Research. 2010;28:1000-6.
679 [33] Simonet WS, Lacey DL, Boyle WJ. Osteoclast differentiation and activation. Nature.
680 2003;423:337-42.
681 [34] Simonet WS, Lacey DL, Dunstan CR, Kelley M, Chang MS, Lüthy R, et al.
682 Osteoprotegerin: A Novel Secreted Protein Involved in the Regulation of Bone Density. Cell.
683 1997;89:309-19.

[35] van Rooijen N, Sanders A, van den Berg TK. Apoptosis of macrophages induced by liposome-mediated intracellular delivery of clodronate and propamidine. Journal of Immunological Methods. 1996;193:93-9.

[36] Fukunaga T, Zou W, Warren JT, Teitelbaum SL. Vinculin Regulates Osteoclast Function. The Journal of Biological Chemistry. 2014;289:13554-64.

[37] Burnett SH, Kershen EJ, Zhang J, Zeng L, Straley SC, Kaplan AM, et al. Conditional macrophage ablation in transgenic mice expressing a Fas-based suicide gene. J Leukoc Biol. 2004;75:612-23.

[38] Arai F, Miyamoto T, Ohneda O, Inada T, Sudo T, Brasel K, et al. Commitment and differentiation of osteoclast precursor cells by the sequential expression of c-Fms and receptor activator of nuclear factor kappaB (RANK) receptors. Journal of Experimental Medicine. 1999;190:1741.

[39] Mackie E, Ahmed Y, Tatarczuch L, Chen K-S, Mirams M. Endochondral ossification: how cartilage is converted into bone in the developing skeleton. International Journal of Biochemistry and Cell Biology. 2008;40:46-62.

[40] Sims NA, Martin TJ. Coupling the activities of bone formation and resorption: a multitude of signals within the basic multicellular unit. BoneKEy Reports. 2014;3.

[41] Flick LM, Weaver JM, Ulrich-Vinther M, Abuzzahab F, Zhang X, Dougall WC, et al. Effects of receptor activator of NFκB (RANK) signaling blockade on fracture healing. J Orthop Res. 2003;21:676-84.

[42] McDonald MM, Dulai S, Godfrey C, Amanat N, Sztynda T, Little DG. Bolus or weekly zoledronic acid administration does not delay endochondral fracture repair but weekly dosing enhances delays in hard callus remodeling. Bone. 2008;43:653-62.

[43] Hartnell A, Steel J, Turley H, Jones M, Jackson DG, Crocker PR. Characterization of human sialoadhesin, a sialic acid binding receptor expressed by resident and inflammatory macrophage populations. Blood. 2001;97:288-96.

[44] Chow A, Lucas D, Hidalgo A, Mendez-Ferrer S, Hashimoto D, Scheiermann C, et al. Bone marrow CD169+ macrophages promote the retention of hematopoietic stem and progenitor cells in the mesenchymal stem cell niche. Journal of Experimental Medicine. 2011;208:261-71.

[45] Husheem M, Nyman JKE, Vääräniemi J, Vaananen HK, Hentunen TA. Characterization of Circulating Human Osteoclast Progenitors: Development of In Vitro Resorption Assay. Calcified Tissue International. 2005;76:222-30.

[46] Sasmono RT, Oceandy D, Pollard JW, Tong W, Pavli P, Wainwright BJ, et al. A macrophage colony-stimulating factor receptor-green fluorescent protein transgene is expressed throughout the mononuclear phagocyte system of the mouse. Blood. 2003;101:1155-63.

[47] Miyake Y, Asano K, Kaise H, Uemura M, Nakayama M, Tanaka M. Critical role of macrophages in the marginal zone in the suppression of immune responses to apoptotic cell–associated antigens. The Journal of Clinical Investigation. 2007;117:2268.

[48] Jacobsen RN, Forristal CE, Raggatt LJ, Nowlan B, Barbier V, Kaur S, et al. Mobilization with granulocyte colony-stimulating factor blocks medullar erythropoiesis by depleting F4/80(+)VCAM1(+)CD169(+)ER-HR3(+)Ly6G(+) erythroid island macrophages in the mouse. Experimental Hematology. 2014;42:547.

[49] Campbell T, Wong W, Mackie E. Establishment of a model of cortical bone repair in mice. Calcified Tissue International. 2003;73:49-55.

[50] Matthys R, Perren SM. Internal fixator for use in the mouse. Injury. 2009;40, Supplement 4:S103-S9.

730 [51] Charles JF, Hsu L-Y, Niemi EC, Weiss A, Aliprantis AO, Nakamura MC. Inflammatory
731 arthritis increases mouse osteoclast precursors with myeloid suppressor function. The Journal of
732 Clinical Investigation. 2012;122:4592-605.
733 [52] Kang J-H, Sim J-S, Zheng T, Yim M. F4/80 inhibits osteoclast differentiation via
734 downregulation of nuclear factor of activated T cells, cytoplasmic 1. Archives of Pharmacal
735 Research. 2017;40:492-9.
736 [53] Lundberg P, Allison SJ, Lee NJ, Baldock PA, Brouard N, Rost S, et al. Greater bone
737 formation of Y2 knockout mice is associated with increased osteoprogenitor numbers and altered
738 Y1 receptor expression. The Journal of Biological Chemistry. 2007;282:19082-91.
739 [54] Wu CA, Pettit AR, Toulson S, Grondahl L, Mackie EJ, Cassady AI. Responses in vivo to
740 purified poly(3-hydroxybutyrate-co-3-hydroxyvalerate) implanted in a murine tibial defect
741 model. Journal of Biomedical Materials Research Part A. 2009;91:845-54.
742 [55] Geissmann F, Gordon S, Hume DA, Mowat AM, Randolph GJ. Unravelling mononuclear
743 phagocyte heterogeneity. Nature Reviews Immunology. 2010;10:453-60.
744 [56] Kaur S, Raggatt LJ, Batoon L, Hume DA, Levesque JP, Pettit AR. Role of bone marrow
745 macrophages in controlling homeostasis and repair in bone and bone marrow niches. Seminars in
746 Cell and Developmental Biology. 2017;61:12-21.
747 [57] Wu C, Orozco C, Boyer J, Leglise M, Goodale J, Batalov S, et al. BioGPS: an extensible
748 and customizable portal for querying and organizing gene annotation resources. Genome biology.
749 2009;10:R130.
750 [58] MacKinnon AC, Farnworth SL, Hodkinson PS, Henderson NC, Atkinson KM, Leffler H, et
751 al. Regulation of alternative macrophage activation by galectin-3. Journal of immunology.
752 2008;180:2650-8.

753 [59] Novak R, Dabelic S, Dumic J. Galectin-1 and galectin-3 expression profiles in classically
754 and alternatively activated human macrophages. Biochimica et biophysica acta. 2012;1820:1383-
755 90.
756 [60] Meesters DM, Neubert S, Wijnands KAP, Heyer FL, Zeiter S, Ito K, et al. Deficiency of
757 inducible and endothelial nitric oxide synthase results in diminished bone formation and delayed
758 union and nonunion development. Bone. 2016;83:111-8.
759 [61] Sakai R, Steck R, Ueno M, Uchida K, Minehara H, Tanaka K, et al. Simulation of the effect
760 of flexible and rigid plate designs on murine fracture healing. Journal of Biomechanical Science
761 and Engineering. 2011;6:311-21.
762 [62] Steck R, Ueno M, Gregory L, Rijken N, Wullschleger ME, Itoman M, et al. Influence of
763 internal fixator flexibility on murine fracture healing as characterized by mechanical testing and
764 microCT imaging. J Orthop Res. 2011;29:1245-50.
765 [63] Ueno M, Uchida K, Takaso M, Minehara H, Suto K, Takahira N, et al. Distribution of bone
766 marrow-derived cells in the fracture callus during plate fixation in a green fluorescent protein-
767 chimeric mouse model. Experimental Animals. 2011;60:455-62.
768 [64] Wynn TA, Vannella KM. Macrophages in Tissue Repair, Regeneration, and Fibrosis.
769 Immunity. 2016;44:450-62.
770 [65] Stutchfield BM, Antoine DJ, Mackinnon AC, Gow DJ, Bain CC, Hawley CA, et al. CSF1
771 Restores Innate Immunity After Liver Injury in Mice and Serum Levels Indicate Outcomes of
772 Patients With Acute Liver Failure. Gastroenterology. 2015;149:1896-909.e14.
773 [66] Nich C, Takakubo Y, Pajarinen J, Ainola M, Salem A, Sillat T, et al. Macrophages-Key cells
774 in the response to wear debris from joint replacements. Journal of Biomedical Materials Research
775 Part A. 2013;101:3033-45.

776 [67] Trindade MCD, Lind M, Sun D, Schurman DJ, Goodman SB, Lane Smith R. In vitro
777 reaction to orthopaedic biomaterials by macrophages and lymphocytes isolated from patients
778 undergoing revision surgery. Biomaterials. 2001;22:253-9.
779 [68] Chavez-Galan L, Olleros ML, Vesin D, Garcia I. Much More than M1 and M2
780 Macrophages, There are also CD169(+) and TCR(+) Macrophages. Frontiers in immunology.
781 2015;6:263.
782 [69] Chow A, Huggins M, Ahmed J, Hashimoto D, Lucas D, Kunisaki Y, et al. CD169(+)
783 macrophages provide a niche promoting erythropoiesis under homeostasis and stress. Nature
784 medicine. 2013;19:429-36.
785 [70] Batoon L, Millard SM, Raggatt LJ, Pettit AR. Osteomacs and bone regeneration (*in press*).
786 Current Osteoporosis Reports. 2017.

787
788
789
790
791
792
793
794
795
796
797
798

Figure legends

Figure 1. CD169 is expressed by endosteal and periosteal macrophages but not by osteoblasts and osteoclast precursors.

A-C) Flow cytometry analysis of enriched endosteal and periosteal cell preparations from long bones of MacGreen mice. **A)** Fold increase in $CD51^+$ osteoblast frequency in endosteal and periosteal cell preparations compared to total BM. **B)** Percent of $CD169^+$ cells within the enriched resident macrophage populations in endosteal and periosteal cell preparations. **C)** Enriched resident macrophage were gated as $F4/80^+Ly6G^-VCAM1^+GFP^{low\text{-}mid}$ cells (left panel red gate and then subsequently middle panel blue gate). Expression of *CD169* (right panel, blue line) within the resident macrophage gate (n = 9). Black lines in right panel show matched isotype control staining. **D)** Non-hematopoietic cells in enriched bone marrow (BM) and periosteal preparations were gated as $F4/80^-CD45^-CD11b^-GFP^-$ (panels left and middle). CD169 expression in these cell populations (right panel, blue line) with black lines representing the matched isotype control. **E)** Osteoclast precursors/progenitors were gated as $B220^-CD3^-Ter119^-CD115^+F4/80^-Ly6C^+$ (left panel. Expression of CD169 in this cell population (middle panel) and a fluorescence minus one (FMO) control (right panel). Data represents mean ± standard deviation of 2 biological repeats and a total of 4 independent samples (each sample represents a pool of 2-3 mice).

Figure 2. $CD169^+$ macrophage depletion resulted in loss of osteomacs and osteoblasts on endosteal bone surfaces in naïve mice.

A) Schematic representing the experimental design including DT/vehicle injection regimen and tissue harvest. **B-C**) Flow cytometric analysis of $F4/80^+Ly6G^-$ myeloid cell (**B,** F^+G^- cells) and $F4/80^+Ly6G^-CD115^{low}CD169^+$ macrophage (**C,** $CD169^+$ cells) frequency in femoral BM at the experimental end point in wild type (WT) and CD169-DTR (DTR) mice treated with vehicle

(DTRx -) or DT (DTRx +). Significance was determined using one-way ANOVA with Tukey's post-test. *, $p<0.05$; **, $p<0.01$; ***, $p<0.001$. Error bars represent standard deviation. **D**) Representative images of IHC staining for F4/80 (left column) and osteocalcin (right column) expression in serial sections of bone in WT mice or CD169-DTR (DTR) mice treated with vehicle (Veh) or DT. $F4/80^+$ osteomac canopy structure (left column, **red arrows**) can be seen associated with $osteocalcin^+$ osteoblasts (right column, **black arrows**) on endosteal diaphyseal cortical bone in all groups except for DT-treated CD169-DTR mice.

Figure 3. Kinetics and quantification of bone and BM impacts of DT treatment in the CD169-DTR mouse model.

A-D) Representative images of IHC staining (brown) for F4/80 (A and C) and Osteocalcin (B and D) expression in sagittal sections of the tibia. Paired images are serial sections representing the diaphyseal region of the tibia on Day 2 after a single DT injection (**A** and **B**) and on Day 4 after 3 DT injections (**C** and **D**) in CD169-DTR mice. All sections were counterstained with hematoxylin. Crosshatch (#) demarks anatomical landmarks in paired serial sections. Original magnification is 20x. **E-F**) Quantification of percent of osteomac/bone surface (OM/BS [%]) **(E)** and osteoblast/bone surface (OB/BS [%] (**F**) on endosteum in WT or CD169-DTR (DTR) mice treated with vehicle (DTRx -) or DT (DTRx +). **G)** Quantification of the number of $F4/80^+$ osteomacs per mm^2 area of periosteum in WT or CD169-DTR (DTR) mice treated with vehicle (DTRx -) or DT (DTRx +). Each data point represents the mean of 3 independent measurements at 3 different sectional depths at least 50 μm apart. Significance was determined using one-way ANOVA with Tukey's post-test. **, $p<0.01$; ***, $p<0.001$. Error bars represent standard deviation.

Figure 4. DT treatment in CD169-DTR mice had no impact on TRAP staining features or osteoclasts frequency but increased serum TRAP activity.

A-D) Representative images of TRAP staining (magenta) in sagittal sections of bone in vehicle (Veh) or DT-treated WT (**A** and **B**, respectively) or CD169-DTR (DTR, **C** and **D**, respectively) mice. $TRAP^+$ multinucleated osteoclasts are indicated by arrows. Original magnification: 20x (**Ai-Di**), 60x (**Aii-Dii**). Scale bar: 100 μm (**Ai-Di**), 20 μm (**Aii-Dii**). **E-I**) Quantification of percent length of TRAP surface (TRAP.S) per bone surface (BS) (**E**), percent area of TRAP staining within the metaphyseal region (**F**), TRAP staining intensity within the metaphyseal region (**G**), unit per liter (U/L) of serum TRAP-5b activity (**H**) and percent trabecular bone (Tb) area within the metaphyseal region (**I**) in vehicle (DTRx -) or DT-treated (DTRx +) WT mice or CD169-DTR mice (DTR). Significance was determined using one-way ANOVA with Tukey's post-test. Each data point represents the mean of 3 independent measurements at 3 different sectional depths at least 50 μm apart. ***, $p<0.001$. Error bars represent standard deviation.

Figure 5. $CD169^+$ macrophage depletion reduced $F4/80^+$ macrophage number within tibial bone injury associated granulation tissue.

A) Schematic detailing the experimental design including timing of DT/vehicle injections and tissue/cell harvest relative to surgery (Tx). **B-C**) Flow cytometric quantification of $F4/80^+Ly6G^-$ myeloid cell (**B**, F^+G^- cells) and $F4/80^+Ly6G^-CD115^{low}CD169^+$ macrophage (**C**, $CD169^+$ cells) number in femoral BM from vehicle or DT-treated CD169-DTR mice. **D**) Percent area of F4/80 staining within the injury site of vehicle-treated (DTR-Vehicle) and DT-treated CD169-DTR (DTR-DT) mice. Each data point represents mean of 3 independent measurements per sample taken at different sectional depths at least 50 μm apart. Significance was determined using two-tailed unpaired t-test. **, $p<0.01$; ***, $p<0.001$. Error bars represent standard deviation. **E-F**) Representative images of IHC staining for F4/80 expression (brown) in tibial injury sites in CD169-DTR mice treated with vehicle (DTR-Vehicle) or DT (DTR-DT). All sections were counterstained with hematoxylin. The bone injury site is demarked by the dotted black box.

Original magnification was 10x and scale bar indicates 200 μm. Abbreviations: CB, cortical bone; and BM, bone marrow.

Figure 6. CD169^{+} macrophage depletion reduced osteomacs and Col1a1^{+} woven bone deposition in tibial bone injury sites.

A) Schematic detailing the experimental design including timing of DT/vehicle injection and tissue/cell harvest relative to surgery (TD). **B-C**) Flow cytometric quantification of F4/80^{+}Ly6G^{-} CD115^{low}CD169^{+} macrophage (**B**, CD169^{+} cells) and F4/80^{+}Ly6G^{-} myeloid cell (**C**, F^{+}G^{-} cells) numbers in femoral BM from vehicle or DT-treated CD169-DTR mice. **D-I**) Representative images of IHC staining for F4/80 (**D-E**, **G-H**, brown) and Col1a1 (**F** and **I**, brown) expression in the tibial injury site of vehicle (**D-F**) or DT-treated (**G-I**) CD169-DTR mice. Osteomacs intercalated throughout woven bone are indicated by black arrows in **E**. Asterisks in **D** and **G** indicate injury adjacent BM. All sections were counterstained with hematoxylin. Original magnifications: 10x (**D, G**) and 40x (**E, H**). Scale bar represents 200 μm in **D**, **G**, **F** and **I** and 50 μm in **E** and **H**. **J**) Percent area of F4/80 staining within the injury site of vehicle-treated and DT-treated CD169-DTR mice. **K**) Percent area of Col1a1^{+} regenerative tissue and Col1a1^{+} fibrotic tissue within the injury site in vehicle-treated and DT-treated CD169-DTR mice. **L**) Percent length of osteoclast surface (Oc.S) per bone surface (BS) in the metaphyseal region of the injured limb. Each data point represents the mean of 3 independent measurements per sample taken in sections at least 50 μm apart. Significance was determined using two-tailed unpaired t-test (*, $p<0.05$ and ***, $p<0.001$). Error bars represent standard deviation

Figure 7. CD169^{+} macrophage depletion reduced the number of galectin-3^{+} macrophages associated with intramembranous ossification in the tibial injury model.

Representative images of dual immunofluorescence staining for F4/80 and galectin-3 expression within the injury site of vehicle-treated and DT-treated CD169-DTR mice (n = 3, experimental

design as per Figure 6A). DAPI nuclear staining is pseudo-colored blue (all panels), F4/80 expression is pseudo-colored red (left and middle panel) and galectin-3 expression is pseudo-colored green (left and right panel). Co-localization is indicated by yellow in the merged image (right panel). Original magnification, 20x; scale bar represents 100 μm.

Figure 8. $CD169^+$ macrophage depletion initiated during the inflammatory phase of fracture repair significantly impaired callus formation.

A) Schematic of the experimental design including timing of DT/vehicle injections and tissue harvest relative to surgery (Fx) as well as how these coincided with fracture healing phase progression [28]. **B-C**) Flow cytometric quantification of $F4/80^+Ly6G^-$ myeloid cell (**B**, F^+G^- cells) and $F4/80^+Ly6G^-CD115^{low}CD169^+$ macrophage (**C**, $CD169^+$ cells) number in femoral BM from vehicle or DT-treated CD169-DTR mice. **D-G**) Representative images of the periosteal injury zone stained with Safranin-O (**D-E**) or for F4/80 expression (**F-G**) from vehicle-treated (**D** and **F**) or DT-treated (**E** and **G**) CD169-DTR mice. Black dotted lines in **D** indicate hard callus with soft callus stained red. Asterisk in **G** indicated BM adjacent to the injury site. Black arrows indicate cortical fracture gap. Original magnification, x4 and scale bars indicate 200 μm. **H**) Quantification of the total callus area (mm^2) in vehicle-treated or DT-treated mice. **I**) Quantification of number of $F4/80^+$ cells per mm^2 of granulation tissue and woven bone within the callus. Each data point represents mean of 3 independent measurements per sample taken at different sectional depths at least 50 μm apart. Significance in **B**, **C**, **H** and **I** was determined using two-tailed unpaired t-test (**, $p<0.01$; ***, $p<0.001$). Error bars represent standard deviation. **J**) Pearson correlation ($r = 0.9$, $p<0.001$) between number of $F4/80^+$ cells within the callus and total callus size (mm^2).

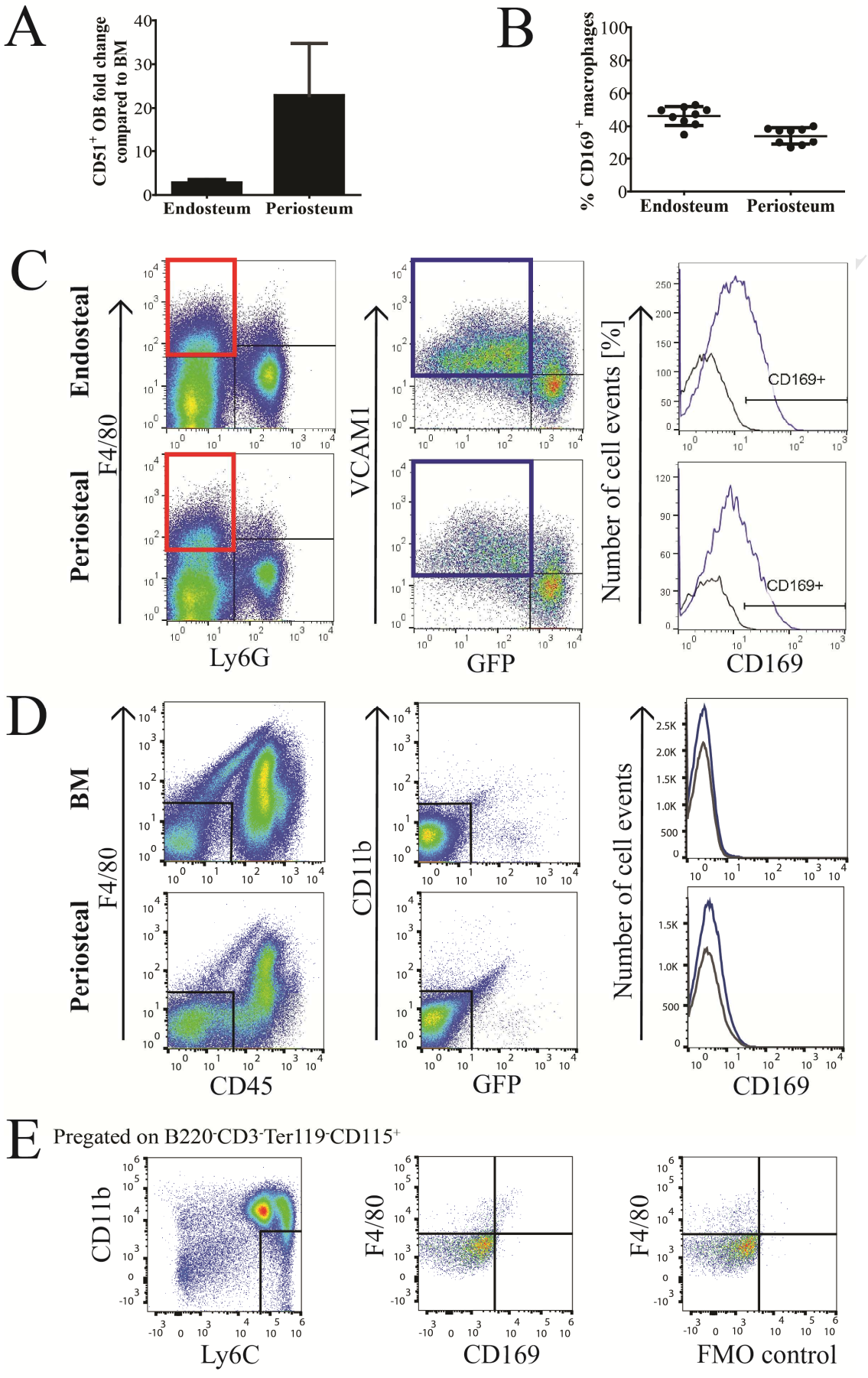
A
CD51+ OB fold change compared to BM
40
30
20
10
0
Endosteum
Periosteum
B
% CD169+ macrophages
100
80
60
40
20
0
Endosteum
Periosteum
C
Endosteal
Periosteal
F4/80
Ly6G
VCAM1
GFP
Number of cell events [%]
CD169+
CD169+
CD169
D
BM
Periosteal
F4/80
CD45
CD11b
GFP
Number of cell events
2.5K
2.0K
1.5K
1.0K
500
0
CD169
E
Pregated on B220-CD3-Ter119-CD115+
CD11b
Ly6C
F4/80
CD169
F4/80
FMO control

Figure 1

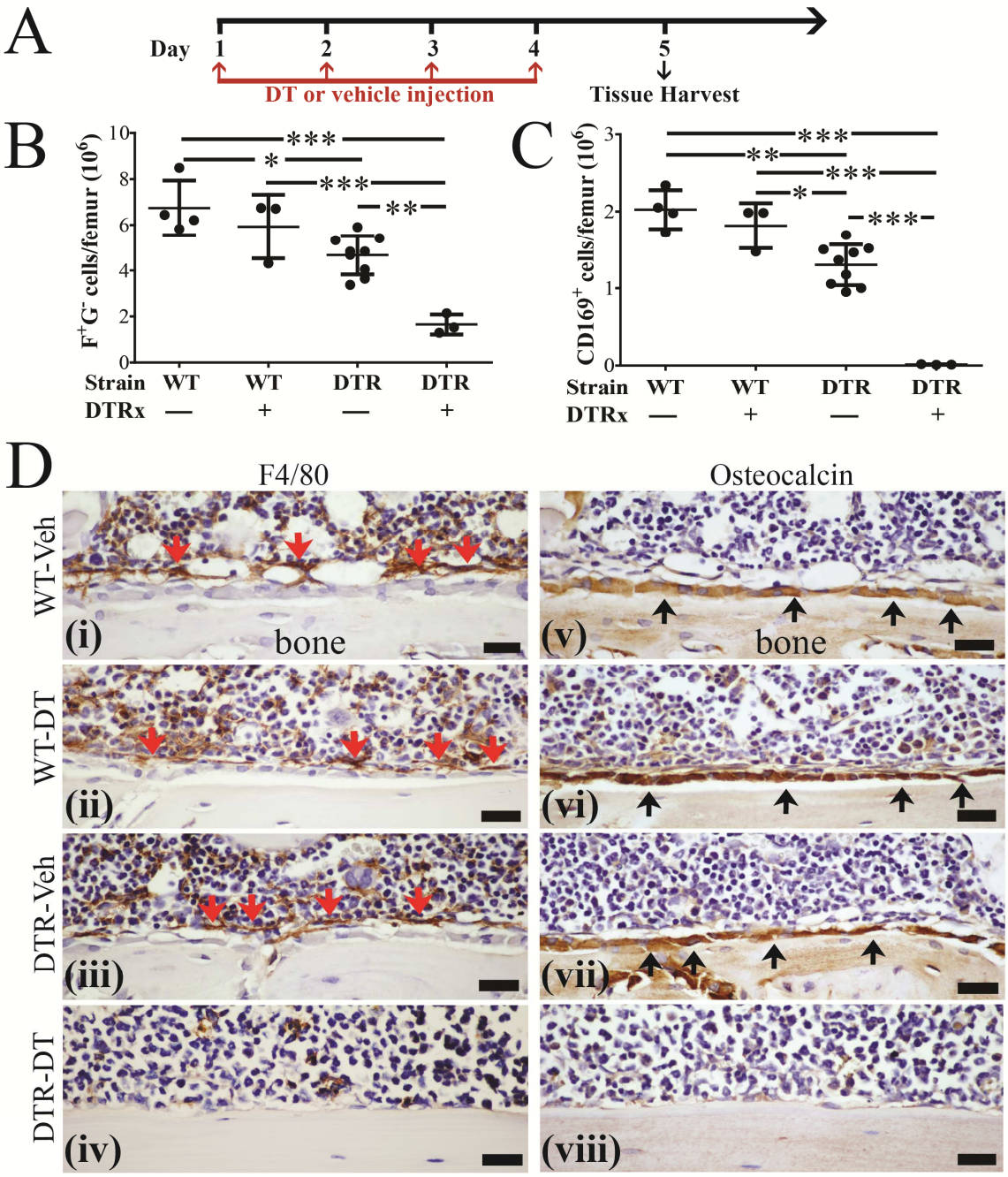
A
Day 1 2 3 4 5
DT or vehicle injection
Tissue Harvest
B
F+G- cells/femur (10^6)
Strain WT WT DTR DTR
DTRx — + — +
C
CD169+ cells/femur (10^6)
Strain WT WT DTR DTR
DTRx — + — +
D
F4/80
Osteocalcin
WT-Veh
WT-DT
DTR-Veh
DTR-DT
(i)
bone
(v)
bone
(ii)
(vi)
(iii)
(vii)
(iv)
(viii)

Figure 2

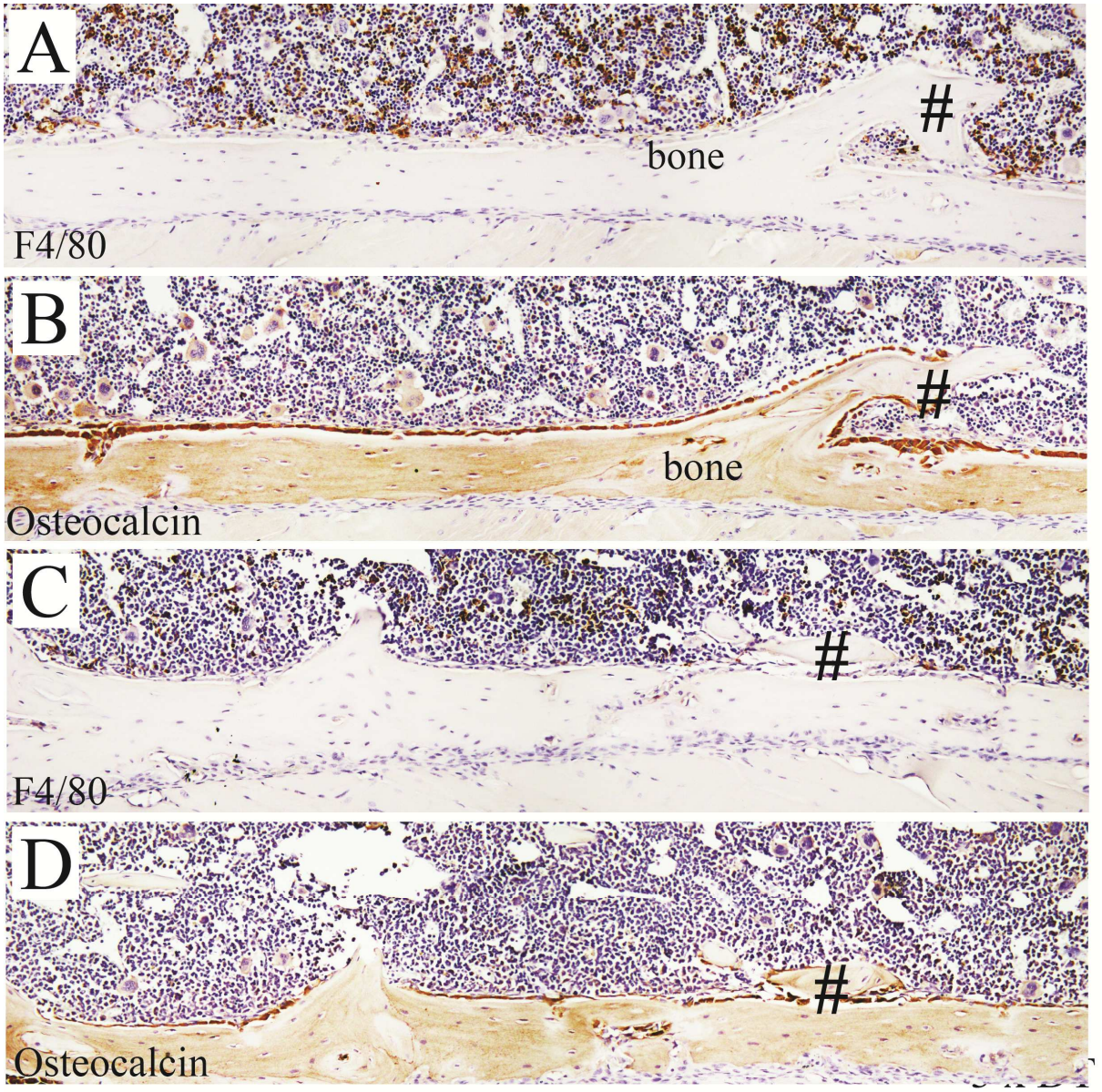
A
bone
#
F4/80
B
bone
#
Osteocalcin
C
#
F4/80
D
#
Osteocalcin

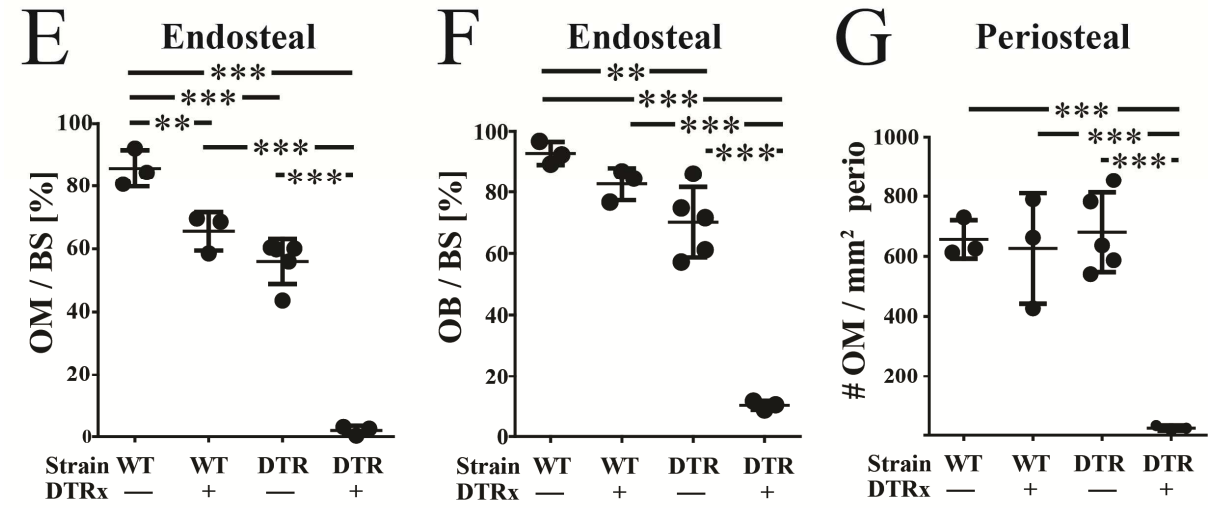
E
Endosteal
OM / BS [%]
F
Endosteal
OB / BS [%]
G
Periosteal
OM / mm² perio
Strain WT WT DTR DTR
DTRx — + — +

Figure 3

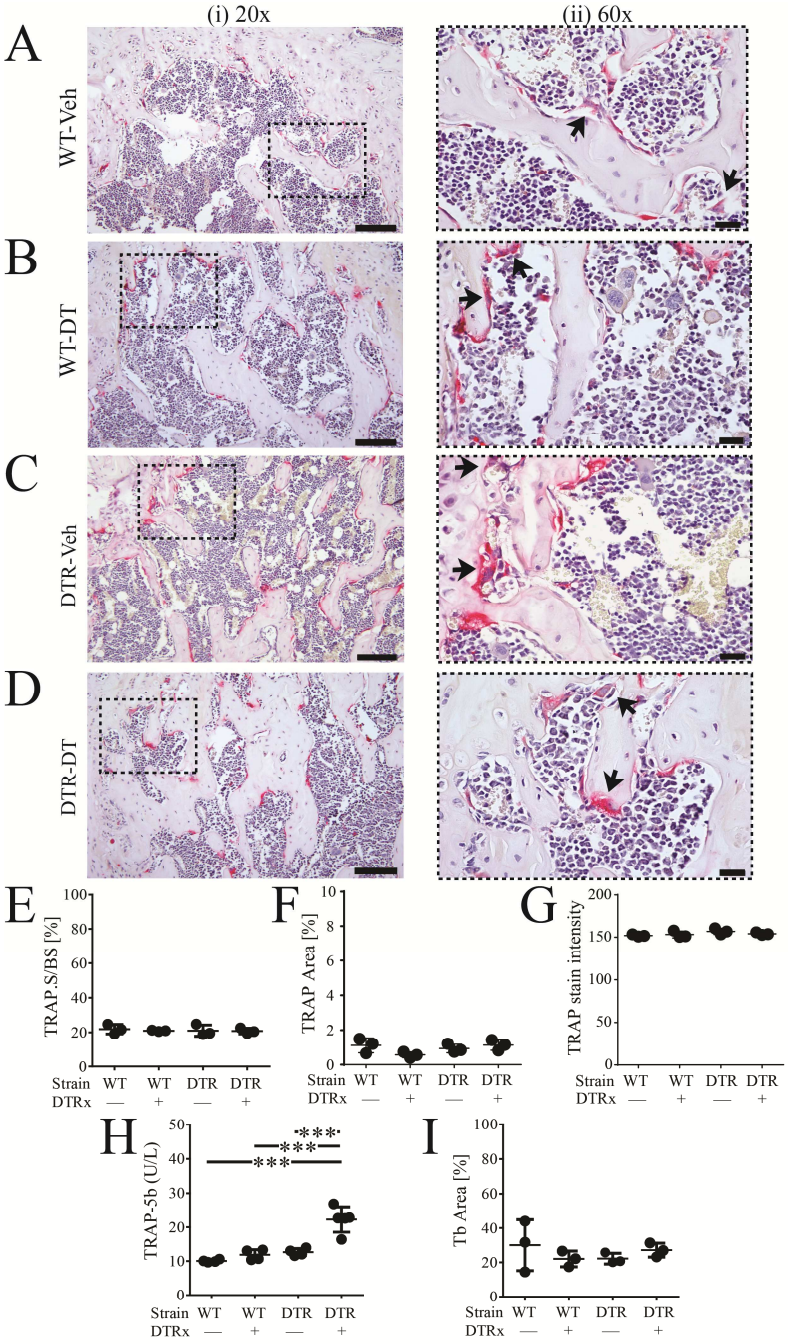
(i) 20x
(ii) 60x
A
WT-Veh
B
WT-DT
C
DTR-Veh
D
DTR-DT
E
TRAP.S/BS [%]
F
TRAP Area [%]
G
TRAP stain intensity
Strain WT WT DTR DTR
DTRx — + — +
H
TRAP-5b (U/L)
***
***
***
I
Tb Area [%]

Figure 4

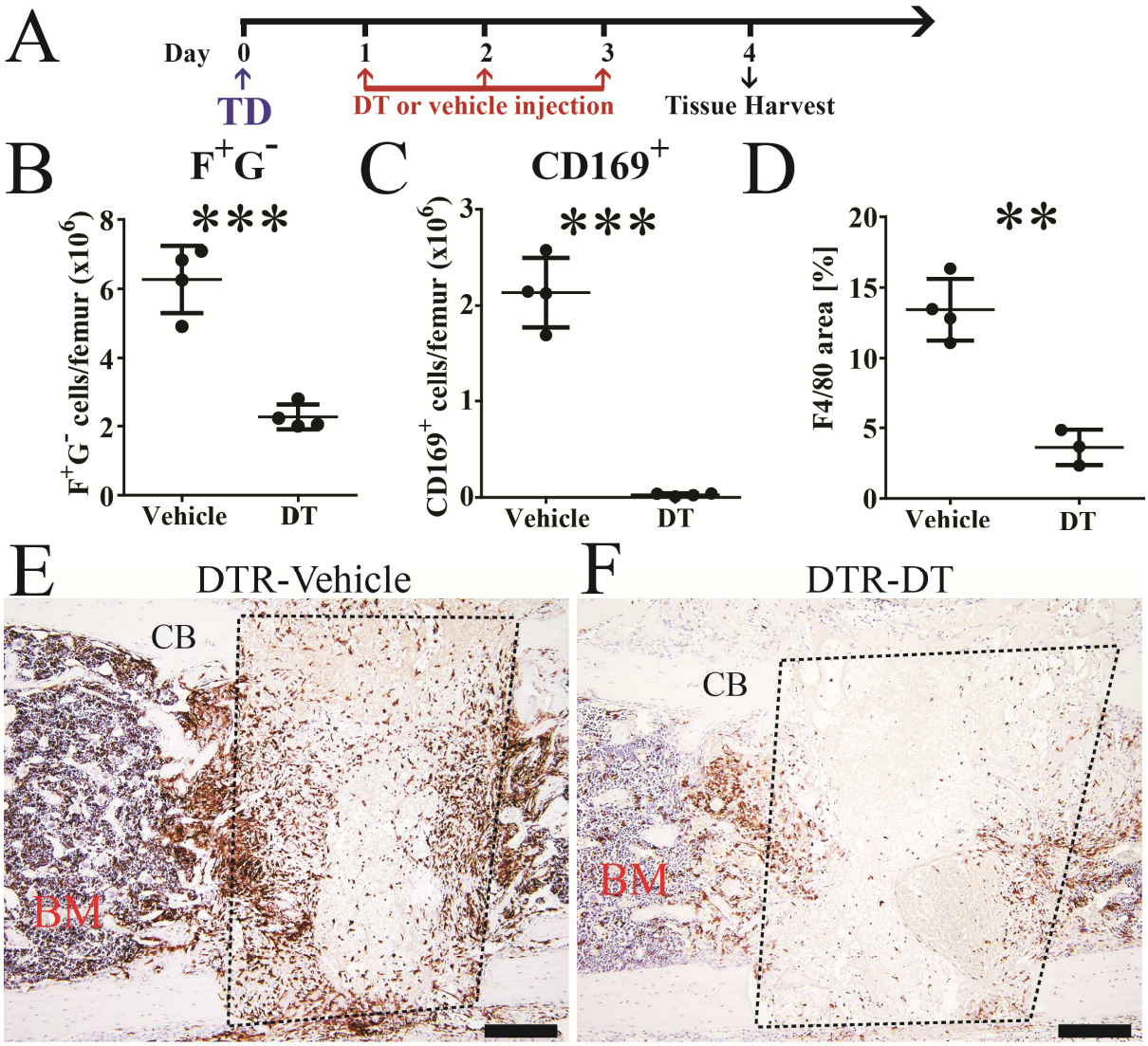

Figure 5

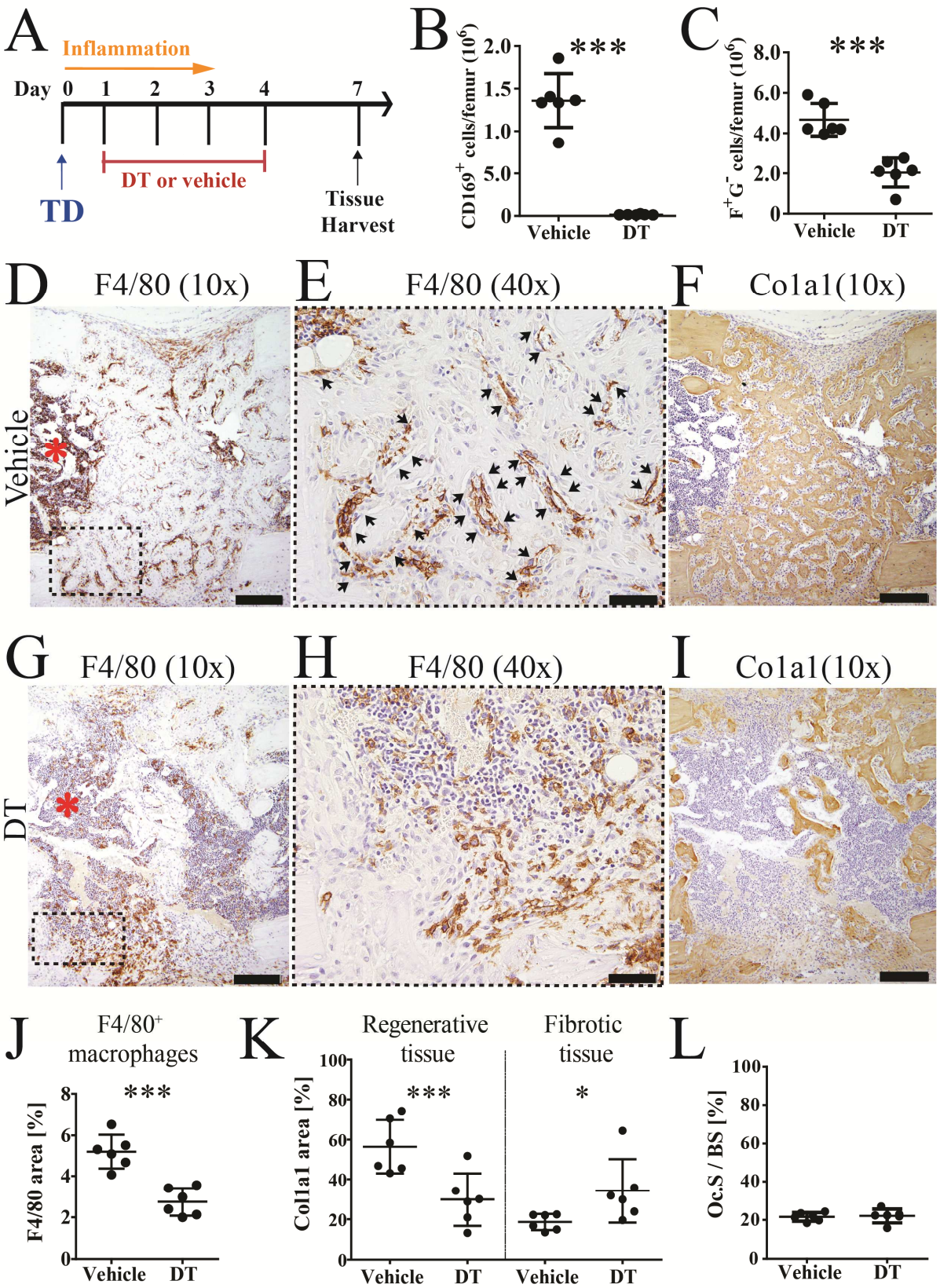
A
Inflammation
Day 0 1 2 3 4 7
DT or vehicle
TD
Tissue Harvest
B
CD169+ cells/femur (10^6)
2.0
1.5
1.0
5.0
0
***
Vehicle
DT
C
F+G- cells/femur (10^6)
8.0
6.0
4.0
2.0
0
***
Vehicle
DT
D
F4/80 (10x)
E
F4/80 (40x)
F
Co1a1(10x)
Vehicle
G
F4/80 (10x)
H
F4/80 (40x)
I
Co1a1(10x)
DT
J
F4/80+ macrophages
F4/80 area [%]
8
6
4
2
0
***
Vehicle
DT
K
Regenerative tissue
Fibrotic tissue
Col1a1 area [%]
100
80
60
40
20
0
***
*
Vehicle
DT
Vehicle
DT
L
Oc.S / BS [%]
100
80
60
40
20
0
Vehicle
DT

Figure 6

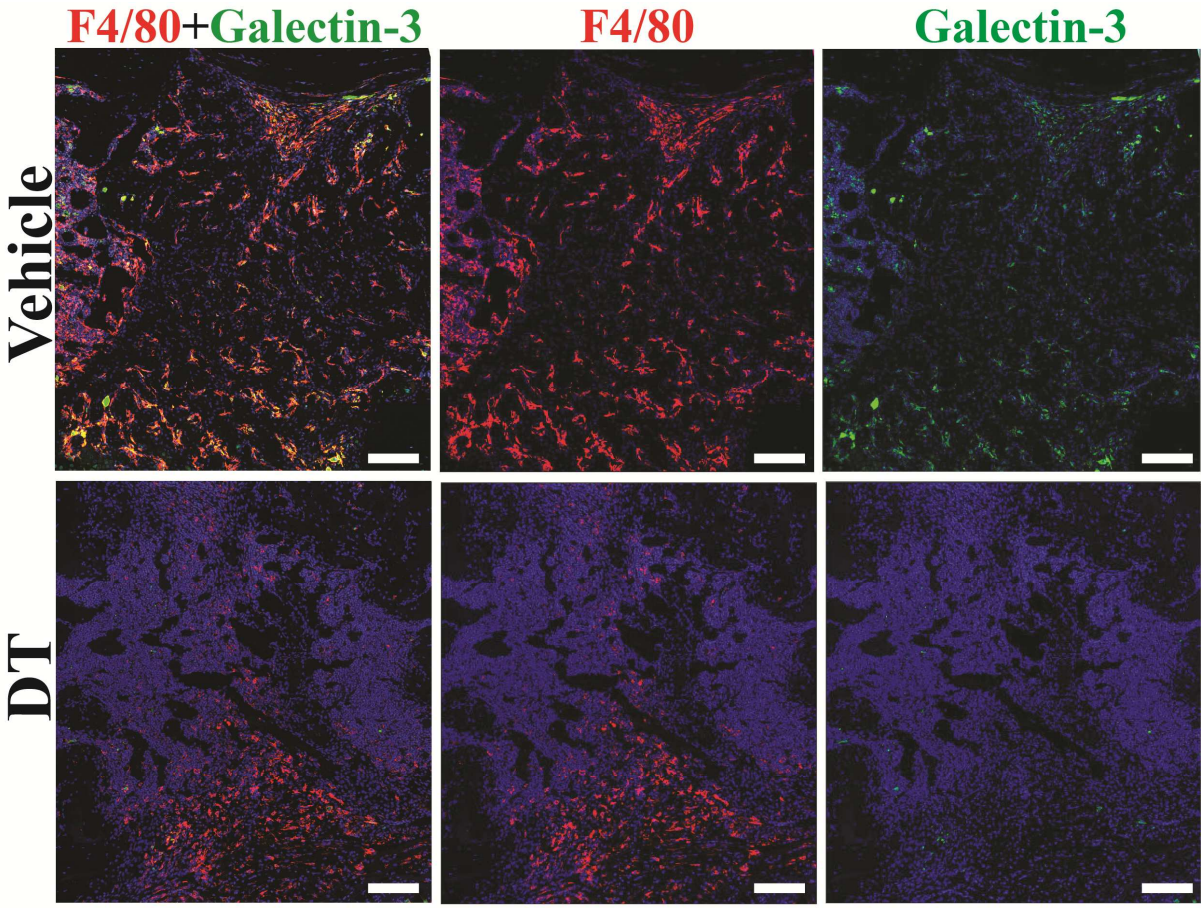

Figure 7

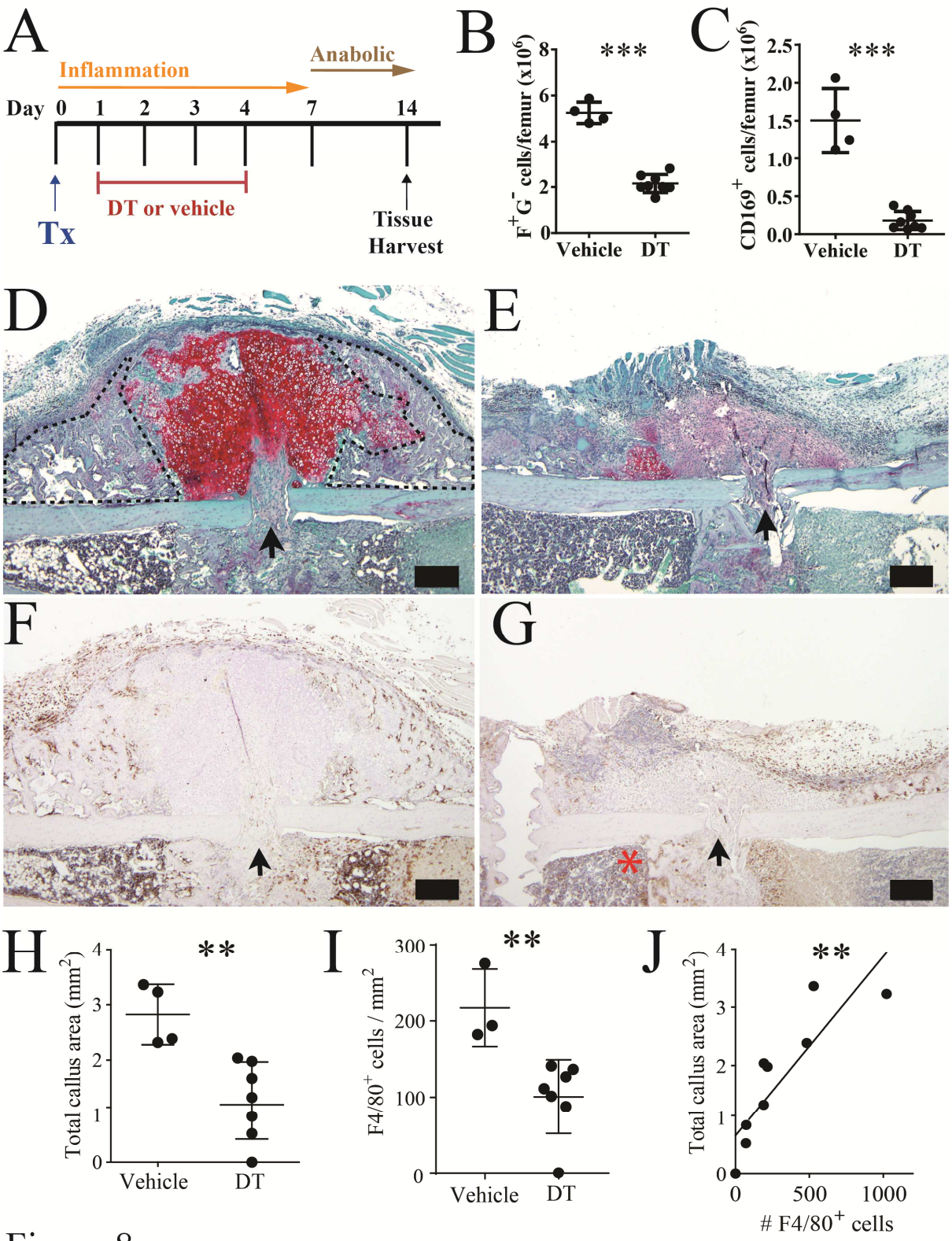
A
Inflammation
Anabolic
Day 0 1 2 3 4 7 14
Tx
DT or vehicle
Tissue Harvest
B
***
F+G- cells/femur (x10^6)
Vehicle
DT
C
***
CD169+ cells/femur (x10^6)
Vehicle
DT
D
E
F
G
H
**
Total callus area (mm^2)
Vehicle
DT
I
**
F4/80+ cells / mm^2
Vehicle
DT
J
**
Total callus area (mm^2)
F4/80+ cells

Figure 8